SBOR: a minimalistic soft self-burrowing-out robot inspired by razor clams

Junliang (Julian) Tao[1*], Sichuan Huang[2] and Yong Tang[3]

[1]*Associate Professor, School of Sustainability and the Built Environment, Center for Bio-mediated and Bio-inspired Geotechnics, Arizona State Univ., Tempe, AZ, 85287, USA
(Corresponding Author) Email: jtao25@asu.edu

[2]Graduate Research Associate, School of Sustainability and the Built Environment, Center for Bio-mediated and Bio-inspired Geotechnics, Arizona State Univ., Tempe, AZ, 85287, USA
Email: shuang64@asu.edu

[3]Graduate Research Associate, School of Sustainability and the Built Environment, Center for Bio-mediated and Bio-inspired Geotechnics, Arizona State Univ., Tempe, AZ, 85287, USA
Email: ytang116@asu.edu

Abstract

We observe that the Atlantic razor clam (*Ensis directus*) burrows out of sand rapidly by simply extending and contracting its muscular foot. This is notably different from its well-known downward burrowing strategy or the dual-anchor mechanism, where closing/opening of the shell and dilation of the foot are also involved. Inspired by this burrowing-out strategy, we design a simple self-burrowing-out robot (SBOR) consisting of a single segment of fiber-reinforced silicone tube actuator and an external control board. The reinforcing fibers limit the motion of the actuator to axial extension/contraction under inflation/deflation. For an actuator that is vertically buried in the sand, cyclic inflation and deflation naturally drives it out of the sand, mimicking the motion of a razor clam. We characterize the burrowing-out behavior of the actuator by varying the actuation period and the relative density (packing) of the sand. Each burrowing cycle features an initial upward advancement during inflation, followed by a downward slip during deflation, resulting in a net upward stride. During the burrowing-out process, the stride length first increases due to a drop in the overburden pressure, the end pull-out resistance, and the side frictional resistance; the stride length then decreases after the top of the actuator moves out of the sand layer, due to a reduction in the effective length of the actuator. The results also indicate that the average burrowing-out speed decreases with the relative density of the sand and changes with the actuation pressure. We developed a simplified model based on soil mechanics to predict the burrowing-out processes in relatively loose dry sands, and the modeling results match well with the experiment results. From this model, the burrowing-out behavior is readily explained by the asymmetric nature of the resistant forces on the two ends of the actuator and the flowing nature of sand upon yielding. Our findings imply that razor clams leverage the natural stress gradient of sand deposits to burrow upward. Another insight is that in order to burrow downward into the sand, additional symmetry-breaking features such as asymmetric geometry, friction, stress state or external load are needed to increase the resistant force (anchorage) in the upward direction and to reduce the resistant force (drag) in the downward direction.

Keywords: razor clam, burrowing, soft robot, soil mechanics

1. Introduction

Compared to locomotion through air or water or over a solid surface, locomotion through soil is much less studied and understood, despite the fact that numerous organisms live underground. In the soil structure, voids exist between solid particles of soil, and this void space can be occupied by fluids such as water, gas or both. Soil behavior thus depends on the particle–particle and particle–fluid interactions. When loaded, soil resists deformation by friction, cohesion and geometric constraints or interlocking. The soil does not seem to be an ideal habitat for a living organism because the energy required for locomotion through soil can be much higher than that required to move through air or water. Yet, the opacity and strength of the soil can protect burrowing animals from predators, extreme temperatures, and adverse environmental conditions (e.g., wind, rain, waves, or snow), and the soil environment can also provide sources of food for these animals. At the same time, underground organisms are often act as ecosystem engineers in that they can modify the physical and chemical environment through bioturbation, bioirrigation and bioerosion (Dorgan 2015; Jones et al. 1997).

Burrowing mechanisms used by a variety of animals were recently reviewed by Dorgan (2015) and Hosoi and Goldman (2015). Among the different burrowing mechanisms employed by limbless organisms, three emerge as the most common. The first is undulatory locomotion, which is used by the sandfish lizard *Scincus scincus* (Maladen et al. 2009), the nematode *Caenorhabdities elegans* (Jung 2010), the burrowing eel *Pisodonophis boro* (Herrel et al. 2011), the opheliid polychaete *Armandia brevis* (Dorgan 2015), and the burrowing wrasses (family Labridae) as described by Tatom-Naecker and Westneat (2018). The second is peristaltic motion, which is used by earthworms (Quillin 1999, 2000). The third is a dual-anchor mechanism that is commonly used by bivalves (Trueman et al. 1966). In addition to the three mechanisms of movement, it was also reported that local fluidization may assist the burrowing processes, as demonstrated by Winter et al. (2012) and the opening of the shell may help reduce the penetration resistance as well (Huang and Tao 2018, 2020).

Soil penetration is also common in plants. Almost all plant roots grow through the soil, and the seeds of some flowering plants also bury themselves in soil for germination. When a plant root grows deeper into the soil, the confining pressure and penetration resistance increases; since the elongation of the tip region would be inhibited by the increased resistance, the tissues in the meristematic region first grow radially, which relieves the stress at the root tip and facilitates the further elongation (Abdalla et al. 1969; Hettiaratchi and Ferguson 1973). The expansion induced stress relief has also been confirmed by numerical and physical experiments (Huang and Tao 2020; Huang et al. 2020). It is also reported that root penetration in soil might be facilitated by circumnutation movements of the root (Del Dottore et al. 2018). Seeds of some flowering plants such as *Erodium* and *Pelargonium* can bury themselves like a corkscrew, which is achieved through the coiling and uncoiling of the awns in response to changes in humidity in the atmosphere and soil (Evangelista et al. 2011; Abraham and Elbaum 2013). The benefit to penetration from root tip rotation was also demonstrated (Bengough et al. 1997; Jung et al. 2017; Tang et al. 2020).

Inspired by the strategies used by animals for locomotion and by plants for growth in granular materials, researchers have developed burrowing robots for a variety of applications: search and rescue, exploration, and soil sampling and monitoring, to name just a few. Recently reported bioinspired burrowing applications include reciprocating drills inspired by the ovipositor drill of wasps (Pitcher and Gao 2015; Gao et al. 2007), dual-anchor or peristaltic burrowing robots inspired by worms (Ortiz et al. 2019; Liu et al. 2019; Rafeek et al. 2001; Isaka et al. 2019), robots inspired by razor clams (Winter et al. 2014), and burrowing devices inspired by root growth (Mazzolai et al. 2010; Sadeghi et al. 2014; Naclerio et al. 2018; Ozkan-Aydin et al. 2019).

While numerous studies have enhanced our understanding of locomotion in granular materials by natural organisms and robots, few studies have focused on reverse locomotion, especially in the vertical direction

(from a deeper location to a shallower location). The question is, after an organism or robot burrows from a higher elevation to a lower one, how does it return to the high elevation?

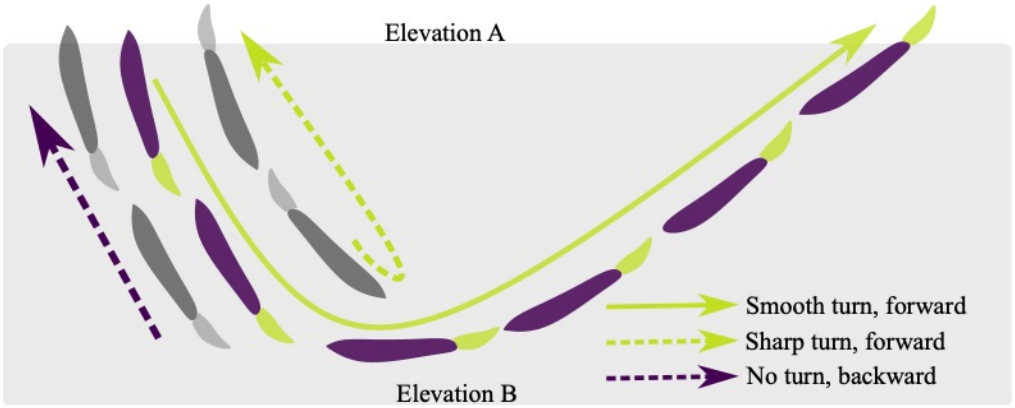

Figure 1. Hypothetical burrowing-out strategies. Sharp turning requires turning at a deep position, followed by forward movement. Smooth turning requires burrowing by forward movement but with a gradual change in the direction of burrowing. No turning is required for direct backward burrowing.

In granular materials, turning can be extremely challenging due to high resistance, especially for slender bivalves with long, rigid shells. There are indeed cases where an organism "turns" smoothly or burrows by changing direction in the soil. For example, lugworms and earthworms are able to construct 'U' shaped burrows (Nash et al. 1984). However, direct turning is not a common strategy. Another option is to rely on reverse or backward locomotion (See the left side of Figure 1). Studies have revealed that backward locomotion on the ground or in the air and water is usually similar to forward locomotion, but with reversed kinematics and a slight change of body posture, as can be found in mole rats (Eilam and Shefer 1992, Eilam et al. 1995), eels (D'Aoüt and Aerts 1999), and hummingbirds (Sapir and Dudley 2012). To the authors' knowledge, the only detailed study of backward burrowing was that of Che and Dorgan (2010), in which the backward locomotion of the polychaeta *Cirriformia moorei* was studied; it was reported that the backward locomotion exhibited the same four phases of forward burrowing and that similar speeds and stress intensities were noted in backward burrowing. The backward burrowing behavior of *C. moorei* only differs from its forward locomotion in terms of the body shape, muscular strength and rigidity of the two ends of the body.

This paper is an extended version of a recently published abstract (Tao et al. 2019) and aims to fill the knowledge gap on the vertical reverse locomotion of razor clams. In Section 2, we report our observations on the burrowing-out behavior of razor clams and show that the clams do not necessarily completely reverse the dual-anchor kinematics when burrowing out of the sand, as some phases of the downward burrowing process are not needed. In Section 3, we demonstrate a clam-inspired minimalistic robot consisting of a one degree-of-freedom extension/contraction soft actuator driven by a pneumatic control board and we discuss its burrowing-out behavior in different sand conditions. In Section 4, we provide a mechanistic explanation of the burrowing-out mechanism with a simplified analytical model based on concepts in soil mechanics. In Section 5, we discuss the limitations and implications of the study and highlight how a vertical reciprocating motion in sand naturally breaks the symmetry, a condition that is required to achieve net translational movement. In Section 6, we provide the conclusions based on the findings of this study.

2. Burrowing-out behavior of razor clams (*Ensis directus*)

2.1. Specimen Collection

Two adult Atlantic razor clams (*Ensis directus*) were collected from a sandbar (located at 41°23'24.0"N, 71°30'36.0"W), near the Point Judith Pond in Narragansett, Rhode Island. When its foot is fully retracted into the shell, the larger clam (C1) measures about 160 mm in length, 22 mm in width, and 15 mm in thickness; the smaller clam (C2) measures 110 mm in length, 15 mm in width, and 10 mm in thickness. The two valves of the shell of these clams curve slightly along the anteroposterior axis, while the curvatures on the dorsal side and the ventral side are similar. The two valves are hinged by a ligament on the lower dorsal edge of the shell. The clam can contract its adductor muscles (which loads the hinge ligament and closes the shell) or relax the adductor muscles (which unloads the hinge ligament and opens the shell). When the clam's foot is fully extended, the portion of the foot that is outside the shell is about 60% of the shell length. The foot extends and contracts during burrowing, and the foot changes shape during the process: the distal part of the foot is spade-like during probing but dilates to a bulb shape during expansion.

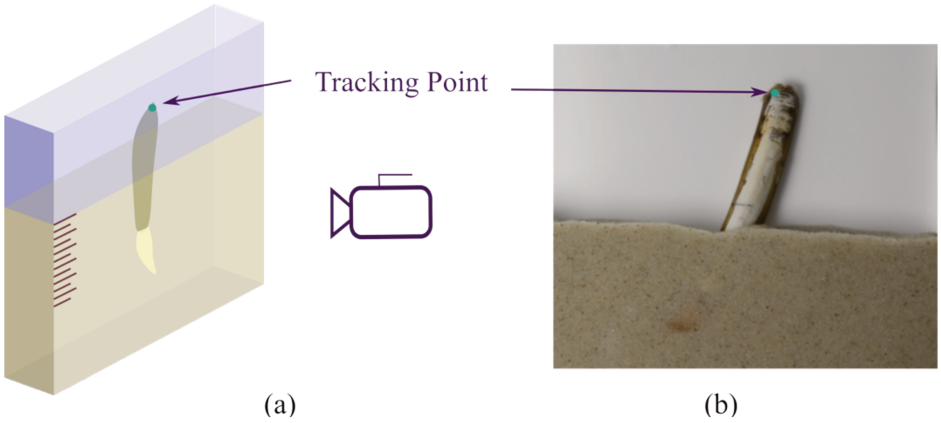

Figure 2. 2D experimental setup: (a) Schematic of the 2D observation chamber, with scaling indicators on the front wall. (b) A razor clam burrowing in Ottawa 20-30 sand.

2.2. Materials and Methods

We observed the burrowing behavior of the two razor clams in two similar laboratory settings. The first series of observations were conducted in the laboratory at Roger Williams University (RWU) in Rhode Island, one day after the clams were collected. Coastal sands were collected and were used in the RWU observations. We used a divider to create a test section in one portion of a clear aquarium tank. The test section, which is similar to a Hele-Shaw cell, measured 250 mm in width, 120 mm in height and 30 mm in thickness (Figure 2). The aquarium was first filled with sea water directly pumped from the ocean. We allowed the sea water to continue circulating to maintain the natural water temperature, and the overflow was directed to a collecting system. Coastal sand sediments (S1) were then poured into the test section to achieve a loose packing of the sand. The two razor clams were then transferred to the testing section and placed on the surface of the sand. A GoPro Hero 4 camera was used to record the burrowing processes at 1920×1080 pixels and 60 frames per second (fps). It was found that the clams did not initiate burrowing activities simply by stimulating their siphons as reported elsewhere (Trueman et al. 1966; Winter et al. 2014). This might be caused by the stress the clams experienced due to transportation and the abrupt change in environment. It was later found that by adding shellfish food to the tank, the clams were stimulated and they responded by burrowing. The burrowing processes usually stopped once the shells were fully buried. To observe burrowing-out behavior, a small amount of table salt was dropped on the sediment directly above the location of the clams. The clams responded by rapidly burrowing out of the sediments.

The same two razor clams were transferred to a laboratory at the campus of Arizona State University (ASU) for another series of observations. The clams were placed in an aquarium maintained at a temperature of

15 °C and a salinity of 25 ppm. The test section in the tank measured 250 mm in width, 250 mm in height and about 30 mm in thickness. Two standard sands, Ottawa F65 sand (S2) and Ottawa 20-30 sand (S3), were used in the experiments (Please see Table 1 for the naming scheme used for the burrowing tests). Both burrowing-in (or downward burrowing, denoted as BD) and burrowing-out (or upward burrowing, denoted as BU) behaviors were observed. The burrowing processes were recorded using a Nikon D3400 digital camera that recorded images at 1920 pixels × 1080 pixels and 30 fps. The camera was calibrated prior to collecting images in order to eliminate any effects from distortions.

Table 1. Naming scheme for razor clam burrowing tests

Symbol	C1	C2	S1	S2	S3	BD	BU
Description	Clam #1 (Length: 160 mm)	Clam #2 (Length: 110 mm)	Sediment #1 (Costal sand)	Sediment #2 (Ottawa F65)	Sediment #3 (Ottawa 20-30)	Downward Burrowing Tests	Upward Burrowing Tests

The recorded videos were processed using the open source computer vision library *OpenCV* (Bradski and Kaehler 2000). An optical flow algorithm based on the Lucas–Kanade method (Lucas and Kanade 1981) was used to track the motion of a point located on the posterior edge of the clam. The natural color and texture of the razor clam shell allowed us to track the motion of this point without the aid of an artificial marker. For each video, the scaling factor—which relates the distance in pixels as measured using the optical flow algorithm to the physical distance moved by the clam during the burrowing process—was determined using an adhesive tape measure that was attached to the front of the tank, which faced the camera (Fig. 2).

2.3. Comparison of Razor Clam Burrowing Tests to Previous Results on Bivalve Burrowing

While the downward burrowing process of razor clams (*Ensis* sp.) has been described in great detail in other studies (Drew 1907; Fraenkel 1927; Trueman 1967), the burrowing-out behavior of razor clams has received far less attention. The only relevant studies identified in the literature were studies that describe the burrowing-out process (described as “emergence” or “recovery” from the sand) for bivalves in other genera: *Cardium (*Ansell 1967*)*, *Mactra* (Ansell and Trevallion 1969) and *Donex* (Ansell and Trevallion 1969; Trueman 1971). No direct observations for *Ensis* were made.

The burrowing characteristics of the razor clams as they burrow in different types of sand are summarized in Figure 3. In the trajectories of the posterior edge of the clams shown in Fig. 3a, the origin represents the original position of the tracking point. For the downward burrowing processes, only the movements after the clam has raised its shell to a vertical position were included. It is clear that most of the time, the clams burrowed in an oblique direction. Thus, the burrowing process can be described either by the total distance of travel or only the vertical component of the movement. Fig. 3b, which presents the vertical burrowing distances that correspond to the trajectories shown in Fig. 3a, gives a better illustration of the burrowing speed and the cyclic, step-wise nature of the burrowing process.

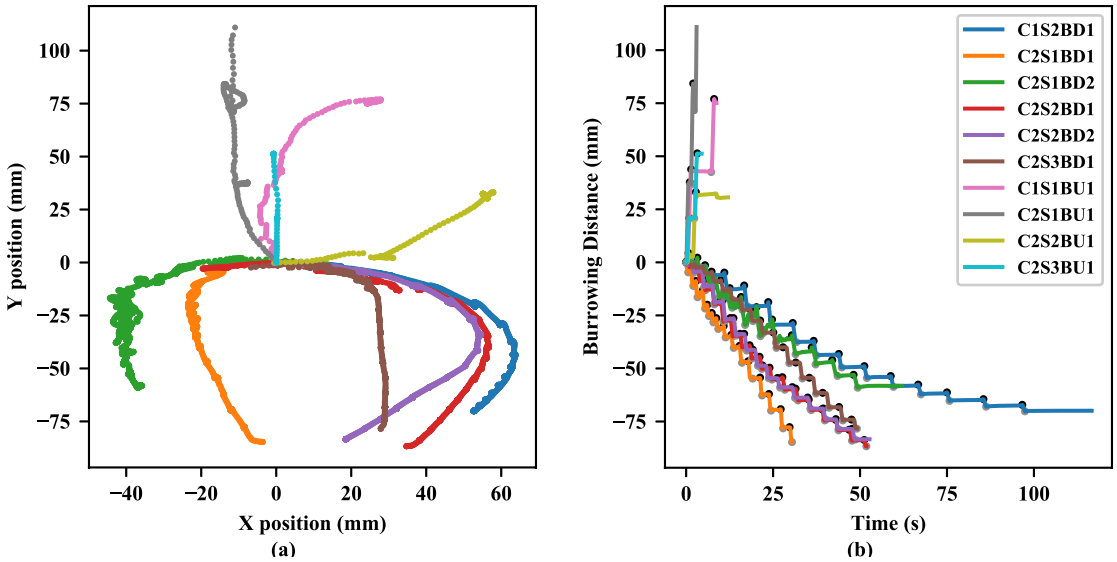

Figure 3. The burrowing characteristics of the razor clam *Ensis directus*: (a) Burrowing trajectory; (b) Burrowing distance. The naming scheme used in each series of tests is provided in Table 1. Videos showing examples of downward and upward burrowing are provided in Supplements S1 and S2.

Figure 4 shows the shell position and foot shape during each of the burrowing steps in a gait cycle for both downward and upward burrowing. Each stride includes an advancement in the direction of motion, followed by a slip in the opposite direction due to insufficient anchorage. The difference in length between the distance advanced and slip is referred to as the *stride length*, and the time difference between the starting points of two consecutive gait cycles is referred to as the *stride period*.

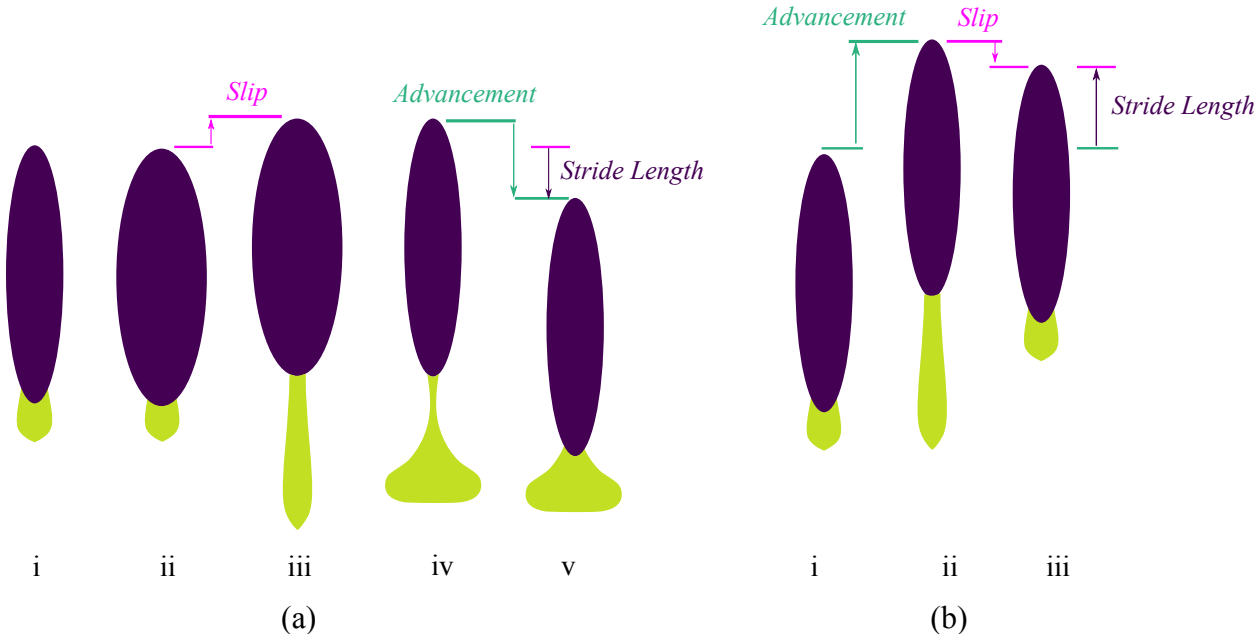

Figure 4. Burrowing "gaits" of razor clams: (a) Downward burrowing gaits, featuring cyclic shell opening (Stage ii), foot extension/probing (Stage iii), shell contraction and foot dilation (Stage iv), and shell retraction (Stage v); (b) Upward burrowing gaits, featuring cyclic foot extension (Stage ii) and foot retraction (Stage iii).

The downward burrowing process by a clam in the genus *Ensis* typically begins when the clam pulls its shell into a vertical position and is assisted by the probing and dilation of the foot to form the first pedal anchor. Next, a series of stepwise burrowing cycles are observed that continue until the shell is fully buried (Fig. 4a). Each downward burrowing cycle continues with opening of the shell to form the penetration anchor (Step ii); probing and extension of the foot (Step iii); closing of the shell, which causes the foot to dilate and form the pedal anchor (Step iv); and retraction of the foot to pull the shell downward (Step v). In downward burrowing, Steps iv and v involve water ejection to facilitate shell movement. All four phases of the burrowing cycle and the corresponding features were observed in our downward burrowing tests and are consistent with the observations by Drew (1907), Fraenkel (1927) and Trueman (1967). The downward burrowing trajectories ($Y < 0$ in Fig. 3) did not collapse to a single curve, which indicates that the trajectories are affected by soil properties as well as the size of the clam. The overall trend in the trajectories was significantly affected by the initial probing stage and the orientation of the formed pedal anchor. The initial posture of the clams is believed to be affected by the soil properties and the pedal strength. The slope of the trajectory curve indicated the direction of motion of the tracking point on the posterior edge of the clam. A common feature for all the downward burrowing trajectories is that the slope of the trajectory curve changed signs at a turning point: prior to reaching this turning point, the shells of the clams rotated significantly; after the turning point, the burrowing mainly consists of translational movement. As the clam burrowed downward, the stride period gradually increased (from 1.5 s to 12 s) and the stride length gradually decreased (from 11.5 mm to 2 mm); these findings are consistent with observations for *Ensis ensis* (Trueman 1967) and other bivalves (Trueman 1983).

In the observations of Atlantic razor clams (*Ensis directus*) that were made in our study, the upward burrowing process shows characteristics that are significantly different than those of the downward burrowing process ($Y > 0$ in Fig. 3). The upward burrowing trajectories indicate that the movements were mainly translational and the direction of movement was coincident with the orientation of the shell. A more striking difference lies in the burrowing speed: it took approximately 10 cycles (from 20 s to 63 s) for the clams to burrow downward for about 50 mm, but it took only about 2 cycles (from 1.6 s to 7.5 s) for them to burrow upward for the same distance. The stride lengths during upward burrowing ranged from 4.5 mm to 46.7 mm (with an average of 30.4 mm), which were considerably larger than those in downward burrowing (which averaged about 5 mm). Videos taken from the side and from above revealed that the size of the opening between the two valves remained constant during the upward burrowing process, which is a marked contrast to the opening/closing of the shell during the downward burrowing process. In addition, the extension of the foot appeared to become more forceful and the extension approached its maximum length (about 60% of the shell length) during some of the upward burrowing cycles; with this forceful extension of the foot, the shell was pushed upward directly (Step ii in Fig. 4b). Subsequently, the foot retracted rapidly, causing a slight downward slip of the shell (Step iii in Fig. 4b). After the foot was fully retracted, it protracted once again, and the burrowing-out cycles continued (back to Step i in Fig. 4b). During the entire process, no expansion of the foot was observed. Comparing the downward and upward burrowing processes, it can be concluded that the upward burrowing process was faster and involved much simpler kinematics: notably, the opening/closing of the shell as well as dilation/contraction of the foot no longer seemed to be necessary.

Some relevant studies examined the upward burrowing behaviors of bivalves in other families such as Cardiidae*,* Mactra and Donax (Ansell 1967 and Trueman 1971). Similar to the behavior of *Ensis* (a member of the family Pharidae), other bivalves burrow out of the sand using cyclic movements, each step of which involves a protraction and extension of the foot, followed by a contraction of the foot. In contrast to *Ensis*, the feet of other bivalves often form a curved shape when they contract, and the subsequent protraction of the foot not only extends but also straightens the foot. From our observations of *Ensis*, the foot extension and contraction both occur along the direction of the shell itself, resulting in a translational movement. Curving and straightening of the foot were indeed observed for the razor clams in our aquarium, but only when the razor clams somersaulted from one point to another across the surface of the sand.

Based on these observations and comparisons, we conclude that the upward burrowing gait of *Ensis* is fundamentally different from its downward burrowing gait, and this conclusion also applies to many other bivalves. In the subsequent sections, we offer a mechanistic explanation of this difference through the use of a bioinspired burrowing robot (as discussed in Section 3) and a simplified analytical model (presented in Section 4).

3. Burrowing-out behavior of a clam-inspired soft actuator

The upward burrowing process of the razor clam can be conceptualized as a single-degree-of-freedom actuator which extends or contracts in the direction of the clam's longitudinal axis. Inspired by this concept, we designed a minimalistic robot consisting of a soft actuator driven by an external control board. The actuator extends and contracts under pressurization and depressurization (Figure 5). We then conducted burrowing tests with this robot under different actuation conditions and in different soil environments.

3.1. Design, Fabrication and Control

As a minimalistic design, the clam-inspired robot includes only one segment of cylindrical, fiber-reinforced, silicone pneumatic actuator. The general fabrication process followed that described in Connolly et al. (2015) and Polygerinos et al. (2017), and necessary modifications were made to suit the purposes of this study. In short, a cylindrical elastomeric tube changes shape and thus generates motion when the inner pressure increases. By reinforcing the tube using inextensible fibers with different wrapping patterns, multiple modes of motion (such as pure motion or combinations of extension, expansion, bending, and twisting) can be achieved (Connolly et al. 2015).

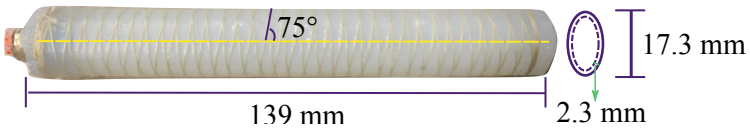

Figure 5. The soft actuator featuring a fiber reinforced silicone tube.

In this study, we selected the two-part liquid silicone Dragon Skin 30 (from Smooth-On, Inc.) to construct the main body of the actuator (which has an inner diameter of 12.7 mm, a thickness of 2.3 mm, and a length of 130 mm). To achieve pure extending/contracting motions, we used a symmetrical, double-helix wrapping of Kevlar fibers at angles of ± 75° to the longitudinal axis of the actuator; we then applied a thin layer of liquid silicone (1.45-mm thick, Dragon Skin 10, also from Smooth-On, Inc.) to the wrapped tube in order to secure the threads.

We used an open-source fluidic control board described by Holland et al. (2014) to drive the actuator. The control board features an Arduino Mega 2560 microcontroller, a Parker D737-23-01 miniature diaphragm air pump, a four-channel MOSFET switch button (Type IRF540 V2.0) from DAOKI, multiple VQ110U-5M pneumatic solenoid valves from SMC Pneumatics, and Honeywell ASDXAVX100PGAA5 pressure sensors. A time-control strategy instead of a pressure-control strategy was adopted due to its simplicity. We controlled the opening and closing time of the valves to achieve inflation (extension) and deflation (contraction) of the actuator. Three actuation periods that are within the range of stride periods for a razor clam were used in each series of tests: T1 = 3.6 s, T2 = 3.0 s and T3 = 1.8 s. During each actuation period T, the valve is opened for the first third of the time period and is closed for the remaining two thirds.

3.2. Calibration Tests in Air

Before conducting the burrowing-out tests in soil, we first tested the performance of the actuator in air. The purpose of the calibration test is twofold: to evaluate the uniformity of the deformations along the axial direction and to back-calculate the equivalent modulus of the actuator. We fixed the top end of the actuator to maintain its vertical alignment. We then tracked the motion of 11 equally spaced markers along the axial direction. We used the same computer vision algorithm (the optical flow algorithm based on the Lucas–Kanade method) to monitor the motion of the actuator under inflation and deflation (Figure 6). Fig. 6a shows the evolution of the internal pressure of the actuators under an actuation period of T3 = 3.6 s as well as the corresponding displacement of tracking point #11 (Point 11), which is located at the bottom of the actuator. It is clear that the actuator behaved elastically and that it takes less time to deflate the actuator (about 0.8 s) than to inflate it (1.2 s). As shown in Fig. 6b, the vertical movement of all tracking points (T3 = 3.6 s) is almost linearly correlated with the vertical position of these points, indicating a nearly uniform deformation along the actuator. To calculate the equivalent modulus of the actuator, we assume that the fiber-reinforced actuator behaves linearly with the inflation pressure. By correlating the maximum deformation of the actuator and the maximum pressure under different actuation periods, we back-calculated the equivalent modulus of the entire actuator, which is about 810 kPa. We also determined the equivalent modulus of the actuator using an alternative approach: we fixed the top end of the actuator and attached standard masses of 500 g, 1,000 g and 1,500 g and measured the deformation of the bottom end of the actuator. With this method, the calculated modulus is about 825 kPa, which is close to that from the pneumatic actuation approach. Note that the modulus of the pure silicone Dragon Skin 30 after curing is about 593 kPa. The fiber reinforcement significantly increases the modulus and make the actuator much stiffer than an actuator made from pure silicone.

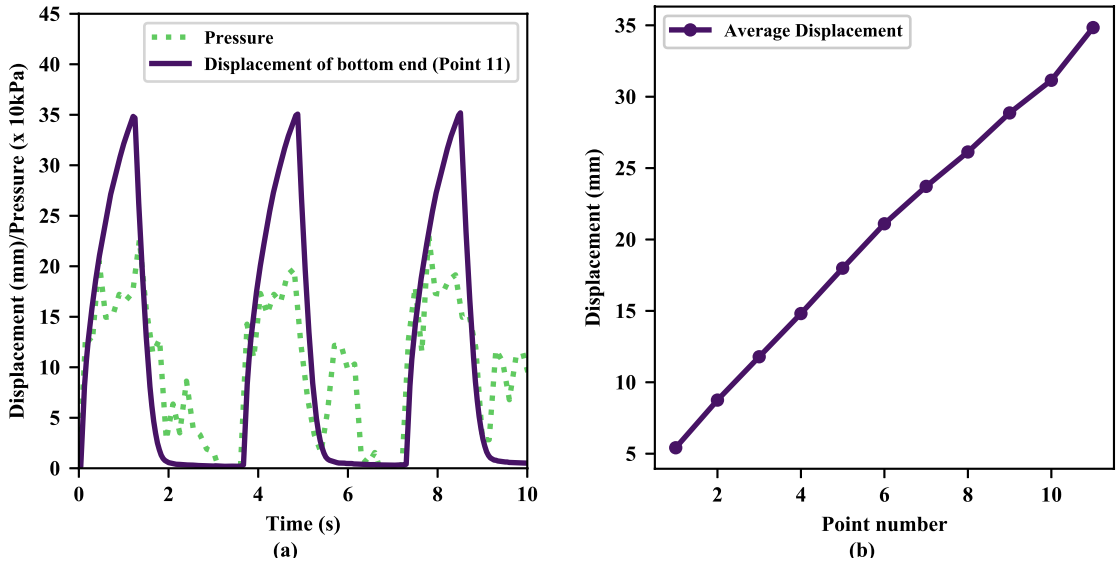

Figure 6. Calibration of the actuator in air: (a) Example curves showing the evolution of pressure and the total deformation of the actuator for T3 = 3.6 s; (b) The displacement of 11 tracking points equally spaced along the actuator for T3 = 3.6 s, where Point 1 is located at the top end of the actuator and Point 11 is located at the bottom end.

3.3. Burrowing-out Tests

Burrowing-out tests were conducted in a cylindrical container with an inner diameter of 406.4 mm and a height of 430 mm (Figure 7). To prepare the sample, a standard procedure was followed for each test. First,

the actuator was connected to a steel tube (with an outer diameter of 3.18 mm and a length of 615 mm). The tube was then passed through the center of a US No. 5 sieve (with a 3.99-mm opening) and a coupler on a holding frame. The sieve was then fixed to the top of the container, and the steel tube was temporarily clipped to the holding frame and the sieve. This procedure ensured the vertical alignment of the actuator and metal tube; it also allowed us to control the initial vertical location of the actuator inside the container. Dry Ottawa F65 sand was then freely pluviated to an empty container through the sieve to achieve a loose packing, and a Syntron VP51D1 vibrator was used to densify the sand samples. By varying the vibrating time, samples with target relative densities (D1: 35%, D2: 45% and D3: 69%) were prepared. The initial embedment depth of the actuator, measured from the soil surface to the top of the actuator, was maintained at 130 mm for all tests. Saturated samples were prepared using a similar procedure, but the sand was pluviated into a container filled with water. The test setup is shown in Fig. 7a. After the completion of the preparation process, the top end of the steel tube was connected to one of the air outlets from the control board, the sieve and clips were removed to free the tube, and the pump was started to initiate the burrowing-out process.

Videos were taken from the side and top of the container during the burrowing-out tests (Figs. 7b and 7c). A marker on the metal tube was used to track the movement of the actuator, and its vertical position was obtained from the side-view video by using the optical flow algorithm based on the Lucas–Kanade method. The soil movement on the surface was observed from the top-view video (Fig. 7c). For each burrowing scenario, three tests were conducted. The test cases were named based on the actuation period T and the sand relative density D. For example, T1D1 indicates that the test was conducted under actuation period T1 (3.6 s) in sand with a relative density D1 (35%). For the tests in saturated samples, the relative density was 45% and the actuation periods were 3.6 s; thus, the corresponding tests under saturation conditions were identified as T1D2S. The naming scheme used for the burrowing tests is provided in Table 2. All results for each burrowing scenario showed great consistency and repeatability.

Table 2. Naming scheme used for robotic burrowing tests

Symbol	**T1**	**T2**	**T3**	**D1**	**D2**	**D3**	**S**
Description	Actuation Period (3.6 s)	Actuation Period (1.0 s)	Actuation Period (1.8 s)	Relative density (69%)	Relative density (69%)	Relative density (69%)	Saturated

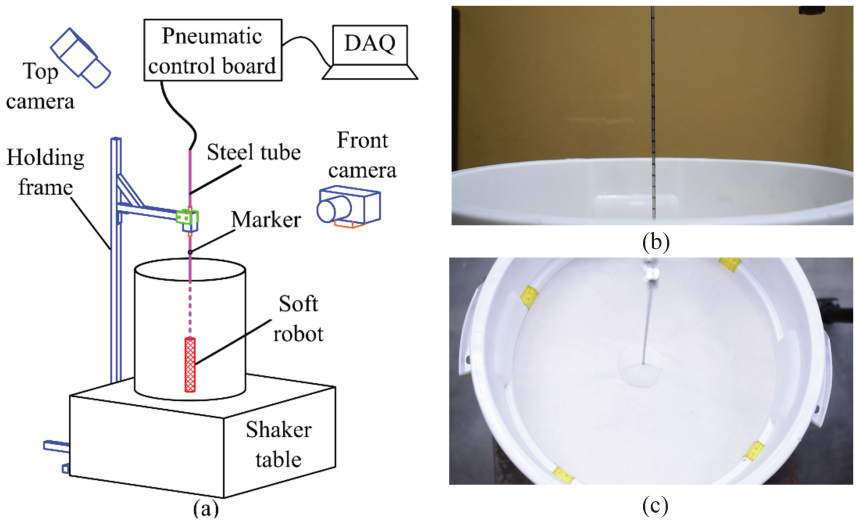

Figure 7. (a) The setup for the burrowing-out tests. Snapshots from the videos: (b) side view and (c) top view. The top view shows the failure surface of the soil mass when the actuator approached the surface.

To better understand the kinematics of the actuator in sand, we conducted a separate 2D chamber test to visualize the movements of the soil around the actuator. The 2D setup was similar to that used to observe the razor clams, except that dry sand is used. The preparation and testing procedure for the 2D test followed that for the cylindrical container tests. Each frame of the video for 2D tests was processed using a dense optical flow algorithm (Farnebäck 2003) in *OpenCV*. Since the sand particles have natural color variations and the pore spaces also present different colors, there are natural textural features (clusters of pixels with different intensities) on each frame of the video. Based on the assumption that the pixel intensity of a particle does not change between consecutive frames and that neighboring pixels will exhibit similar motion, the entire velocity field of the pixels can be obtained by comparing two consecutive frames. One can then use the pixel velocity field to infer the sand particle velocity field.

3.4. Results for Burrowing-out Tests with the Robot

3.4.1. Burrowing cycles, advancement, slip, and stride length

The results for the burrowing cycles, advancement, slip, and stride length for the robot are shown in Figure 8. The evolution of the inner pressure of the actuator in response to the valve state is shown in Fig. 8(a), and a representative burrowing-out curve is shown in Fig. 8(b). It can be noticed that the burrowing-out curve for the robot resembles the burrowing curves for the razor clam in Fig. 3(a) in the sense that the burrowing process is also cyclic and stepwise. For each burrowing cycle, the actuator advances during inflation and slips during deflation. It is observed that the actuator advances during the entire duration of the first 1/3 of T, but it only slips for about 22% of the total duration of T, which indicated a "rest" period (equivalent to 45% of the total duration of T) that lasts until the end of each cycle. These observations on the durations of the inflation process and deflation process were consistent with those from the calibration tests (Fig. 6(a)).

Similar to the description of the burrowing processes of clams, we refer to each burrowing cycle as a *gait cycle* and we refer to the upward movement, downward movement, and net movement in each cycle as the *advancement*, *slip*, and *stride length*, respectively, which we collectively refer to as *characteristics*. The stride length is simply the difference between the advancement and the slip. Fig. 8(c) shows the characteristics of the burrowing process for Case T1D2. The advancement and slip both increase in subsequent cycles; however, the advancement increases faster at an earlier stage, while the slip increases faster in the later stages. This causes the stride length to first increase and then decrease. Comparing the stride length curves to the video footage, it is found that the turning points occur one to two cycles before the top end of the actuator emerges from the sand.

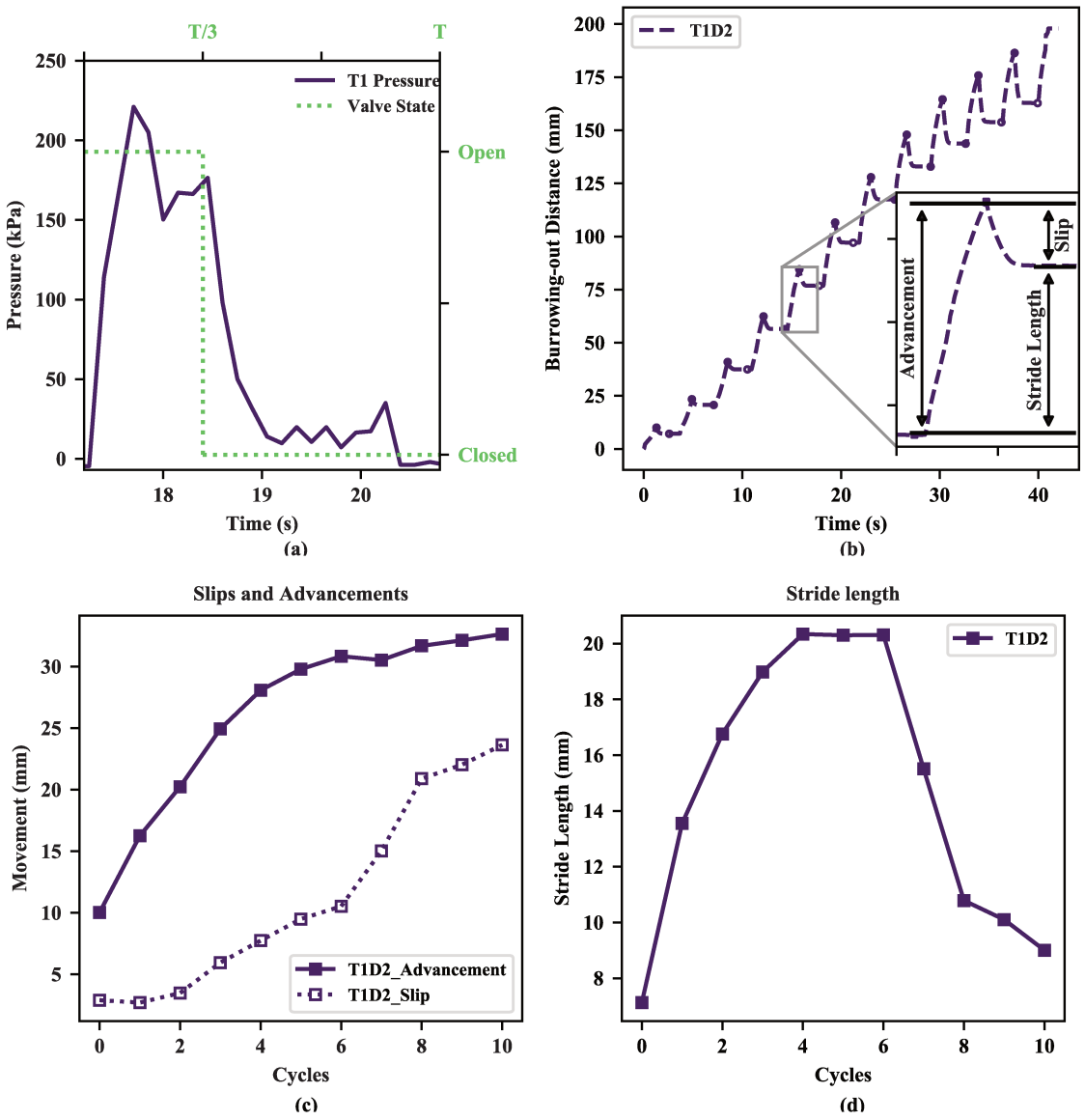

Figure 8. (a) Representative pressure curve in one cycle and the corresponding value states (shown is an example case of T1). (b) A representative burrowing-out curve and definitions of burrowing characteristics. (c) The evolution of the advancements (solid symbols) and slips (empty symbols) for Case T1D2. (d) The evolution of the stride length for Case T1D2.

3.4.2. Anatomy of a burrowing cycle: 2D test results

From the 2D test, the movements of the sand particles around the actuator can be visualized. A video showing the burrowing process overlaid with the color-coded velocity field can be found in the supplement (in Section S3). Figure 9 shows the normalized velocity field of the sand around the actuator at different time points during a given cycle. At the start of inflation, sand particles near the actuator (in a triangular region in the 2D representation) suddenly move down temporarily (Fig. 9(a)); immediately after, the bottom end of the actuator moves downward (Fig. 9(b)) and the top end moves upward (advancement, in Figs. 9(c) and 9(d)). These movements continue until the end of inflation (Fig. 9(e)). Note that during the inflation process, the downward movement of the bottom end of the actuator during slip is significantly shorter than the movement observed at the top end of the actuator during advancement.

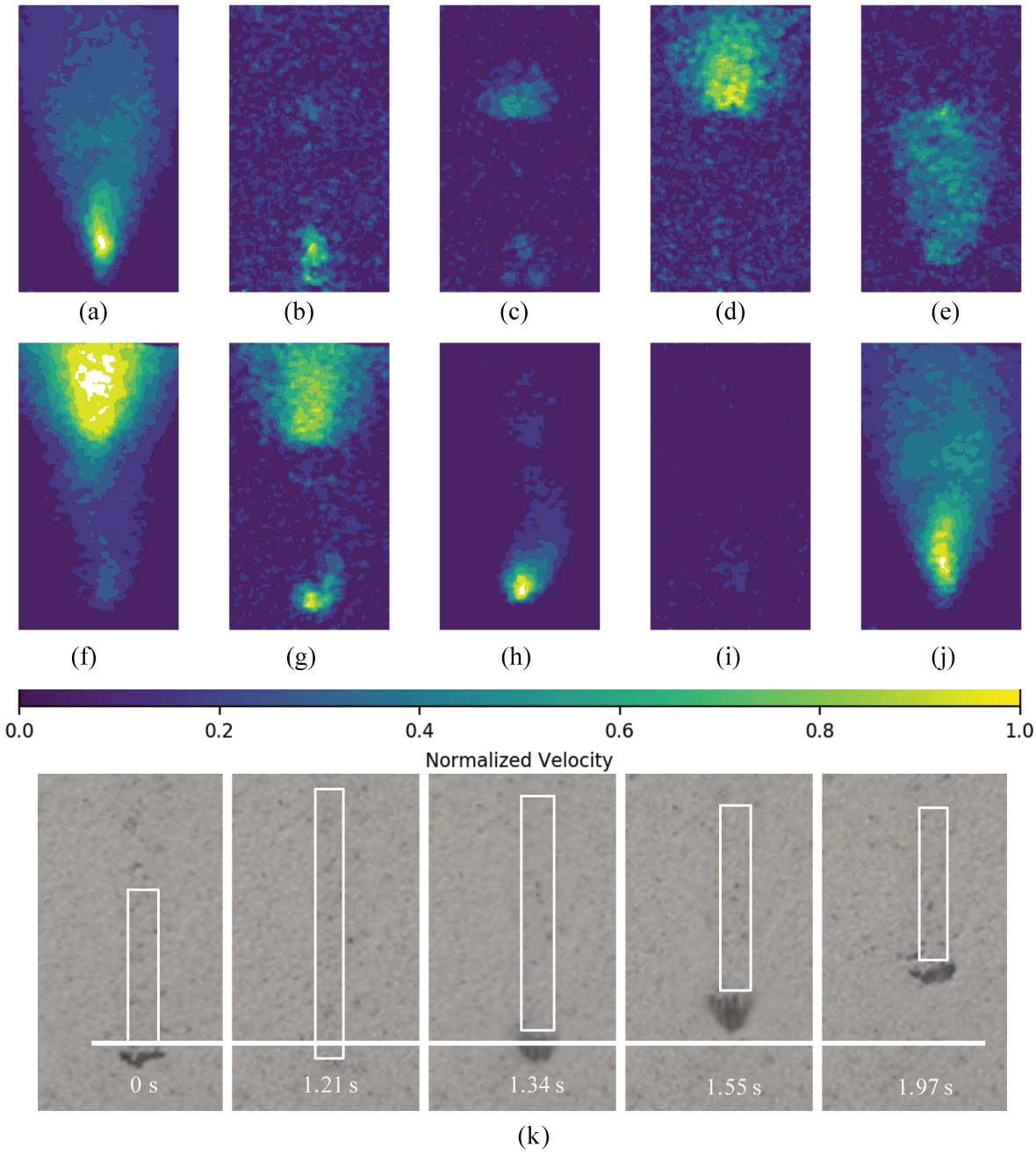

Figure 9. Particle movement during one burrowing-out cycle (the period T3 = 3.6 s). The pixel velocity field is normalized for each frame, so the color indicates the relative velocities at each time instant. The relative timing of each frame is: (a) At 0 s, inflation starts and the sands move downward slightly; (b) at 0.042 s, both ends move inward and the bottom end moves faster; (c) at 0.084 s, both ends move inward and the top end moves faster; (d) at 0.46 s, only the top end movement is visible; (e) at 1.21 s (about 1/3 of T1), which is the end of inflation and the start of deflation, the sands move downward slightly; (f) at 1.26 s, both ends move inward and the top end moves faster; (g) at 1.34 s, both ends move inward and the bottom end moves faster; (h) at 1.55 s, the top end stops moving and only the bottom end moves upward; (i) at 1.97 s (about 55% of T1), the bottom end stops moving and the rest period starts; (j) at 3.586 s, the rest period ends and another cycle starts. (k) Snapshots of the 2D chamber highlight how the flowing sand has backfilled voids due to the upward movement at the bottom end of the actuator during deflation.

In the early stage of deflation (Figs. 9(f)– 9(h)), the downward movement of the sands at both ends of the actuator can be observed: at the top end, the sands simply settle due to the downward movement of the top end of the actuator (slip); at the bottom end, the upward movement of the bottom end of the actuator creates void space underneath, and the surrounding sand particles flow into the space due to gravity. The movements continue until the completion of the deflation process (Fig. 9(i)). Note that in the earlier stage of the deflation process, the sand particles at the top end move faster than those at the bottom end (Fig. 9(f)); however, in the later stage, the sand particles at the bottom end move faster (Fig 9(h)). Afterwards, there is a rest period which lasts until the next cycle starts (Fig. 9(j)). Snapshots of the 2D chamber (Fig. 9(k)) highlight how the flowing sand has backfilled the voids due to the upward movement at the bottom end of the actuator during deflation.

3.4.3. Effects of actuation period/pressure, relative density and saturation

Figure 10 summarizes the results related to the effects of actuation period/pressure, relative density and saturation. Fig. 10(a) summarizes all the burrowing curves for different burrowing scenarios, and Figs. 10(b) and 10(c) illustrate the corresponding burrowing characteristics. It is clear that the burrowing characteristics change with the actuation period as well as the relative density and the saturation state of the sand.

Comparing the results for Cases T1D1, T2D1 and T3D1, it is found that the advancements, slips and stride lengths all increase with the actuation period T. This can be attributed to the fact that different actuation periods lead to the development of a different amount of pressure in the actuator, and a higher pressure results in a higher elongation of the actuator. Actuation periods T1, T2 and T3 show a maximum pressure of 197.5 kPa, 186.5 kPa, and 150.3 kPa, respectively. Although the stride length is the smallest for Case T3D1, the overall burrowing out speed (7.7 mm/s) in this case is higher than that for Case T1D1 (5.98 m/s) and Case T2D1 (6.55 m/s); this is because the resting time in each cycle of T3 is the shortest of all actuation periods.

Comparing results for Cases T1D1 and T1D2, it is found that the advancements, slips and stride lengths all decrease with the packing or relative density of the sand. This is mainly due to the fact that the higher the relative density, the higher the strength and stiffness of the sand. With the same level of actuation pressure, the resistance experienced by the actuator is higher. It is interesting that the burrowing curve for test T1D3 is significantly different from those in Cases T1D1 and T1D2. Repeated tests reveal that it took about 10 cycles for the actuator to 'break' the soil. Before the breaking-through point, the advancements, slips and stride lengths were all very small. The stride length gradually increased with cycles until the actuator broke through, at which point the advancements, slips and stride lengths all increased dramatically. After breaking through, the maximum stride length for T1D3 (22.5 mm) was even greater than that for T1D1 (21.3 mm) and T1D2 (20.3 mm).

Comparing the test results for Cases T1D2 and T1D2S, the effect of saturation can be assessed. In general, the advancements in Case T1D2S are smaller than those in Case T1D2. For the first three cycles in Case T1D2S, the advancement decreases and the slip is higher than that in Case T1D2. Afterwards, the slip in Case T1D2S becomes smaller than that in Case T1D2. These trends result in smaller strides overall in Case T1D2S and, notably, decreasing strides in the first three cycles. The maximum stride length in Case T1D2S (12.7 mm) is about 38% smaller than that in Case T1D2 (20.3 mm).

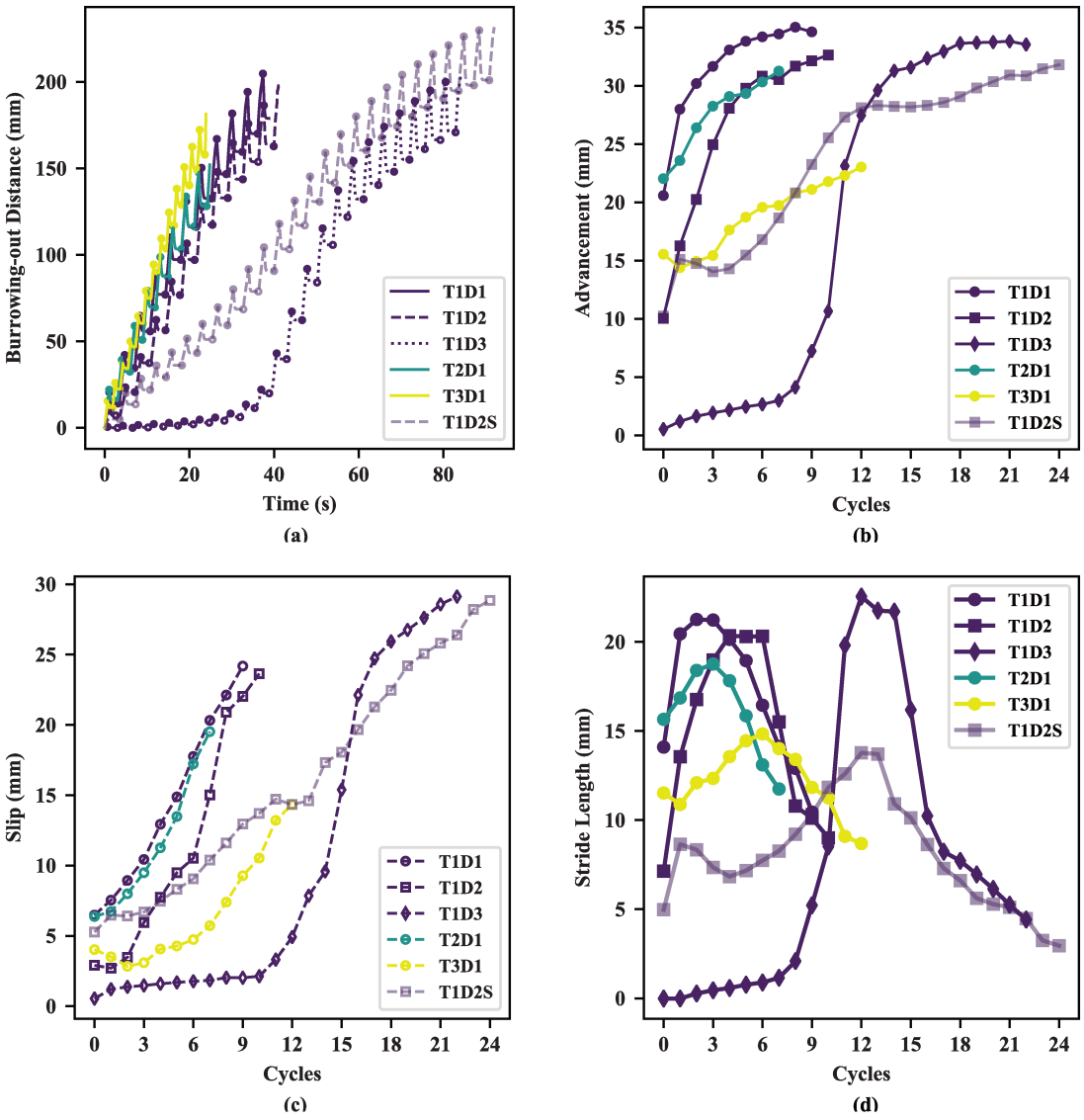

Figure 10. (a) Summary of all burrowing curves for different burrowing scenarios (one representative curve for each burrowing scenario is included). (b) Advancements, (c) slips, and (d) stride lengths. Curves shown in different colors highlight the effect of the actuation period T, with T1 = 3.6 s (purple); T2 = 3.0 s (green) and T3 = 1.8 s (yellow). The curves shown in purple with different symbols highlight the effect of the sand's relative density D, with D1 = 35% (circles); D2 = 45% (squares); and D3 = 69% (diamonds). The saturated case T1D2S uses the same color and symbols as the dry case T1D2, but with a semi-transparent effect. The naming scheme used in the test series can be found in Table 2.

The exact reasons for the breakthrough behavior in Case T1D3 and the decreasing strides in the first several cycles in Case T1D2S are not readily apparent. We will provide some insights about this in Section 5.1, where we discuss the analytical model.

4. A Simplified Analytical Model

4.1. Assumptions and Simplifications

We attempt to model the advancement and slip during each cycle in a quasi-static equilibrium framework. Specifically, we assume a steady-state movement during inflation and deflation and neglect the inertia effect. This treatment significantly simplifies the modeling process and only requires the force–deformation relationship; the time-varying features such as velocity and acceleration are not considered. The core idea of the proposed model is 1) to establish the equation of equilibrium of the actuator; 2) to calculate the tensional stresses along the actuator; and 3) to calculate the resulting strain and deformation/movement. From the 2D chamber tests, we learned that during inflation, both ends of the actuator move away from a certain point along the actuator; during deflation, both ends move toward another point along the actuator. These particular points, which do not move during the corresponding inflation or deflation cycles, are called *anchor points*. For different cycles, the anchor points change location along the actuator due to changes in forces.

We also make the following assumptions for further simplification:

- A1: The change of inner pressure results only in extension or contraction in the axial direction of the actuator, and no other modes of motion (e.g., twisting or expansion) occur.
- A2: The actuator is assumed to be a linear elastic composite, where the length of the actuator changes linearly with the inner pressure and where the deformation of the actuator does not cause a change in the actuator thickness and modulus.
- A3: From Fig. 9, it can be noticed that the inflation process in relatively shallow and loose sand is dominated by the upward movement of the top end of the actuator, while the downward movement of the bottom end is negligible. Therefore, the anchor point during inflation is assumed to be located at the bottom end of the actuator.
- A4: The elongation of the actuator caused by inflation is fully recovered during the deflation process.
- A5: The soil is homogeneous, and its properties do not change during the burrowing process.
- A6: The friction coefficient at the soil–actuator interface is a constant and isotropic, i.e., the friction coefficients in the upward and downward directions are the same and do not change during the process.
- A7: The confining pressure (lateral contact stress) on the actuator surface is proportional to the embedment depth, and it remains unchanged during the burrowing process.

To simplify the modeling of the burrowing process, we divided the process into two distinct phases: in the first phase, the actuator is fully buried in the sand. In the second phase, the actuator is only partially buried, once the top end of the actuator has emerged from the sand. Each phase includes cycles of inflation and deflation, which can also be considered separately.

4.2. Main Components of the Analytical model

For modeling purposes, the two phases of the burrowing-out process (the fully buried phase and the partially buried phase mentioned above) are modeled separately. The cycles of inflation and deflation in the two models are also modeled separately. Therefore, a total of four models are developed for the analytical model to consider the following conditions: 1) fully buried inflation, 2) fully buried deflation, 3) partially buried inflation, and 4) partially buried deflation. A schematic for the four models is provided in Figure 11.

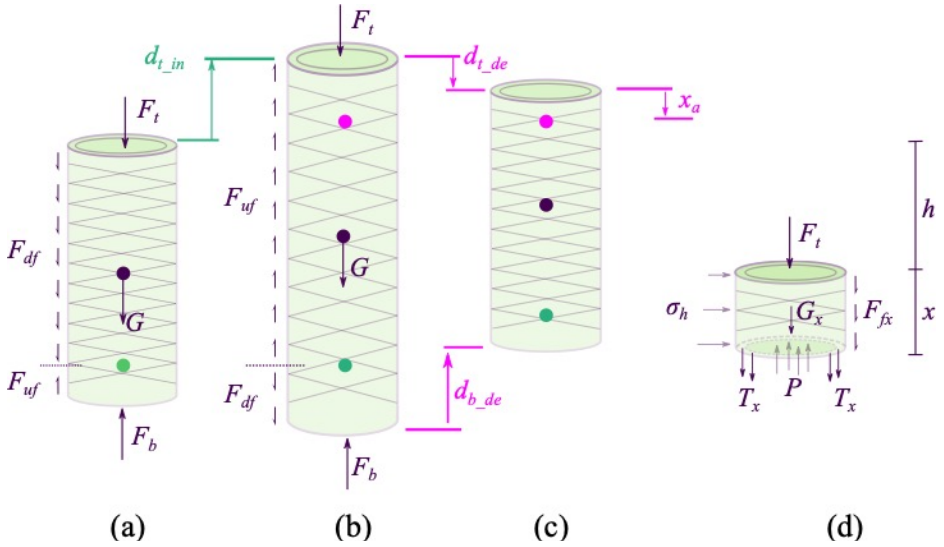

Figure 11. Schematic for the simplified model: (a) The initial state of the actuator and the external forces on the actuator during the inflation process, (b) the inflated state of the actuator and the forces on the actuator during the deflation process, (c) the deflated state of the actuator, and (d) the stresses/forces on a segment of the actuator. The green dot represents the anchor point during inflation, the pink dot denotes the anchor point during deflation, and the brown dot denotes the center of gravity.

4.2.1. Inflation process in the fully buried phase

Figs. 11(a) and 11(b) show the actuator before and after inflation, respectively. The green point shows an assumed anchor point. The external forces experienced by the actuator include the forces from the sand at the top and the bottom of the actuator (F_t and F_b, respectively); the gravitational force G; and the downward and upward frictional forces from the sand (F_{df} and F_{uf}, respectively). However, in the proposed model below, the anchor point during inflation is assumed to be located at the bottom of the actuator; thus, F_{uf} would have a value of 0. This assumption is made since during each cycle, the downward movement of the bottom end of the actuator only lasted for a short period of time, and its total movement was extremely small (as shown in Fig. 9). Assuming that the top end of the actuator is the origin and that the positive direction points downward, the equation of equilibrium reads as follows:

$$F_{df} + F_t + G = F_b \tag{1}$$

The tensional force along the actuator (Fig. 11(d)) is then:

$$T(x) = P_{in} \cdot A_a - F_t - F_f(x) - \frac{x}{L}G \tag{2}$$

where x is the distance measured from the top end of the actuator, A_a is the inner cross-sectional area of the actuator, P_{in} is the inflation pressure, L is the original length of the actuator, and $F_f(x)$ is the total frictional force from the top end of the actuator to the point of interest.

The total extension of the actuator, which is also the distance traveled during the advancement of the top end, d_{t_in}, can then be calculated as:

$$d_{t\_in} = \Delta L = \int_0^L \frac{T(x)}{E \cdot A_s} dx \tag{3}$$

where E is the modulus of the actuator and where A_s is the area of the solid cross section of the actuator.

F_t is the force needed to move the actuator upward and to cause failure of the soil above it. In geotechnical engineering, F_t is also referred to as the *uplift capacity*, the *pull-out capacity*, or the *inverse bearing capacity*; the methods for estimating F_t are widely explored for geotechnical engineering applications such as ground anchors and uplifting pile foundations. Here, we adopt the method developed for shallow circular anchors with an embedment depth less than seven times the diameter of the circular anchor (Giampa et al. 2016). This method assumes that uplifting a circular anchor causes failure of the soil above the anchor. The uplifting resistance includes the self-weight of the soil of failure and the shear resistance along the failure surface. In its simplest form, $F_t = N_\gamma \cdot \gamma h \cdot A$, where γ is the unit weight of the sand; A is the total cross-sectional area of the actuator, where $A = A_a + A_s$; h is the embedment depth or the distance from the sand surface to the top end of the anchor (or the actuator in this study); and N_γ is the breakout factor, which is related to soil strength parameters (critical state friction angle ϕ_c and peak dilation angle ψ_p), anchor diameter (D), and embedment depth (h). The critical friction angle represents the friction angle at a critical state where the soil experiences full structure degradation and when soil deformation can continue without causing changes in stress and volume. The dilation angle represents the particle interlocking effects; it changes with the relative density of the sand and depends on the confining pressure. In general, the higher the relative density and the lower the confining pressure, the higher the dilation angle. For shallow sand deposits or sands with lower confining pressures, Giampa and Bradshaw (2018) and Chakraborty and Salgado (2010) provide a convenient method to correlate relative density and confining pressure to the peak dilation angle. (See Supplement S9 for the complete expression of N_γ in Equation (S22); see Supplement S8 for details on the methods used to estimate the peak dilation angle (Equation (S21)). The value for F_t can then be predicted based on ϕ_c, D_r, γ, h and A.

The frictional force $F_{df}(x)$ can be calculated using Equation (4).

$$F_{df}(x) = \int_0^x \mu_d \cdot \sigma_h \cdot 2\pi R \cdot dx = \int_0^x \mu_d \cdot [K_0 \gamma (h + x)] \cdot 2\pi R \cdot dx = \pi R K_0 \gamma \mu_d (2hx + x^2) \quad (4)$$

where μ_d is the downward sand–actuator interface friction coefficient corresponding to the upward movement of the actuator, σ_h is the lateral confining earth pressure along the actuator, and R is the outer radius of the actuator. The lateral confining earth pressure σ_h can be estimated from the vertical earth pressure ($\gamma(h + x)$) through the at-rest lateral earth pressure coefficient, K_0, $\sigma_h = K_0 \gamma (h + x)$, where K_0 is a function of the peak friction angle of the soil and where $K_0 = 1 - \sin\phi_p$. The peak friction angle of the soil depends on the critical friction and the dilation angle, $\phi_p = \phi_c + \beta\psi_p$, where β is a fitting parameter. Substituting the above expressions into Eq. (4), and then substituting Eq. (4) into Eqs. (2) and (3), the advancement during the inflation process can be estimated by

$$d_{t\_in} = \Delta L = \frac{L}{E \cdot A_a}\left[P_{in} \cdot A - N_\gamma \cdot \gamma h \cdot A - \pi R K_0 \gamma \mu_d \left(hL + \frac{1}{3}L^2\right) - \frac{1}{2}G\right] \quad (5)$$

Equation (5) clearly illustrates that the advancement is determined by the positive contribution from the inflation pressure and the negative contributions from the strength of the soil, the interface friction and the self-weight of the actuator. After each burrowing cycle, both embedment depth h and the breakout factor N_γ decrease, leading to decrease in end pull-out resistance and side frictional resistance. The overall effect is a significant increase in the advancement d_{t_in}.

4.2.2. Deflation process in the fully buried phase

In contrast to the inflation process (shown in Figs. 11(b) and 11(c)), the movements of both ends of the actuator are significant, and neither is negligible. Thus, it is necessary to determine the anchor point, which does not move during the deflation process. Again, assuming that the top end of the actuator is the new origin and the positive direction points downward, the equation of equilibrium is as follows:

$$F_{df} + F_t + G = F_b + F_{uf} \tag{6}$$

where F_{uf} is the upward frictional force caused by the downward movement of the segment above the anchor point and where F_{df} is the downward frictional force caused by the upward movement of the segment below the anchor point.

Following a similar procedure shown above for the inflation process, F_{uf} and F_{df} can be expressed in terms of lateral earth pressure, friction coefficient, contact area and embedment depth; similarly, the distribution of stresses along the actuator can be estimated and, thus, the movement of the top end (d_{t_de} or slip) and the bottom end (d_{b_de}) can be estimated. In contrast to the inflation process, the anchor point during the deflation process in each cycle needs to be determined by solving a deformation compatibility equation (Equation (7)) invoked by Assumption A4.

$$d_{t\_\mathrm{de}} + d_{b\_de} = d_{t\_in} \tag{7}$$

The resulting slip during the deflation process is determined to be

$$d_{t\_de} = \frac{1}{E \cdot A_a}\left[\frac{1}{3}\pi R K_0 \gamma \mu_u {x_a}^3 + \left(\pi R K_0 \gamma \mu_u h' - \frac{G}{2L'}\right){x_a}^2 + (P_{de} \cdot A - \gamma h' \cdot A)x_a\right] \tag{8}$$

where μ_u is the upward sand–actuator interface friction coefficient corresponding to the downward movement of the actuator; $h' = h - d_{t\_in}$ and $L' = L + d_{t\_in}$ are the updated embedment depth and actuator length after the inflation process, respectively; x_a denotes the location of the anchor point and is the distance measured from the top end of the actuator; and P_{de} is the deflation pressure, which is equal to the inflation pressure.

Equation (8) clearly illustrates that the slip depends on the location of the anchor point x_a, which depends on the soil, the actuator, and the actuation properties. After each burrowing cycle, both anchor position x_a and embedment depth h' change, leading to an increase in slip d_{b_in}. However, since the slip increases at a slower rate than the increase in the advancement (Eq. (5)), the stride length increases before the top end of the actuator emerges from the sand surface.

4.2.3. Burrowing process in the partially buried phase

The general procedure for deriving the advancements and slips for the burrowing cycles in the partially buried phase is similar to that for the fully buried phase. A key difference is that we treat the partially buried actuator as two segments: the top segment, which is above the sand surface, freely extends and contracts; the bottom segment, which is below the sand surface, behaves as a fully buried actuator with an updated length (which is shorter than the original length). Due to the reduction in the effective embedded length of the actuator, the stride length decreases after the top end of the actuator emerges from the sand surface.

Based on the above procedures, for each inflation cycle, the corresponding advancement can be calculated; this advancement is then used to update the embedment depth for the subsequent deflation cycle, for which the resulting slip can be calculated. Afterwards, the slip is used to update the embedment depth for the next inflation cycle, and the calculation continues until a completion criterion is met. The criterion can be a

particular threshold stride length or a target burrowing distance. The entire modeling process is implemented in Python.

4.2.4. Input parameters

The input parameters for the proposed model include soil properties, actuator properties, soil–actuator interface properties, actuation and initial conditions. Soil properties include maximum and minimum void ratio (e_{max}, e_{min}), relative density (D_r), critical state frictional angle (ϕ_c) and peak dilation angle (ψ_p); actuator properties include the self-weight (G), length (L), outer diameter (D), inner diameter (D_{in}), Young's modulus (E); soil–actuator interface frictional coefficients, which include downward and upward coefficients (μ_d and μ_u, respectively); the actuation pressures, which are the inflation and deflation pressures (P); and the initial condition, which is the initial embedment depth (h). Most of these parameters are readily available. Efforts have been made to determine soil properties following standard soil mechanics testing procedures. The maximum and minimum void ratios (e_{max}, e_{min}, respectively) are determined following ASTM standards D4253 and D4254. The critical state frictional angle for Ottawa F65 sand can be determined by triaxial tests and has been reported elsewhere (Badanagki 2019). The dilation angle can be determined using the models of Bolton (1986), Chakraborty and Salgado (2010), and Giampa et al. 2018); we followed the procedures in Chakraborty and Salgado (2010) and Giampa et al. (2018) to account for the low confining pressure encountered at shallow depths. The frictional coefficients were determined using the sliding block method (described in Section S6 of the Supplement). The Young's modulus of the actuator was determined using both inflation and tensile testing methods, as described in Section 3.2. Since the inflation pressure was not a constant value, the equivalent modulus was back-calculated using the maximum pressure during inflation in the calibration tests. To be consistent, we also used the measured maximum pressures under different actuation periods as the inputs for the inflation and deflation pressures in the model. A summary of the input parameters is provided in Table 3. Additional details on the determination of these parameters can be found in the supplement (in Sections S5 through S8).

Table 3. A summary of input parameters used in the model

Soil Properties		**Actuator Properties**		
Relative density (D_r)	0.35	Weight (G)		0.5 N
Maximum void ratio (e_{max})	0.79	Length (L)		130 mm
Minimum void ratio (e_{min})	0.56	Outer diameter (D)		17.3 mm
Critical state frictional angle (ϕ_c)	31.75	Inner diameter (D_{in})		12.7 mm
Specific gravity (G_s)	2.65	Modulus (E)		827 kPa
β *	0.62	Actuation pressures (P)	T1	197.5 kPa
Soil–actuator Interface Properties			T2	187.5 kPa
Upward friction coefficient (μ_u)	1.0		T3	150.3 kPa
Downward friction coefficient (μ_d)	1.0	Initial embedment depth (h)		130 mm

* β correlates the peak friction angle ϕ_p with the critical friction angle ϕ_c: $\phi_p = \phi_c + \beta\psi_p$.

4.3. Model Validation

Figure 12 shows the comparison between the calculated burrowing characteristics and the experimental results (for Cases T1D1, T2D1 and T3D1), highlighting the effects of the actuation period/pressure. Qualitatively, the model captures all the observed trends (evolution of the slips, advancements and stride lengths under different actuation pressures) in the experiments. For Cases T1D1 and T2D1, the model

underestimated the advancements (up to 6%) in the fully buried phase, but it slightly overestimated these motions in the partially buried phase (up to 7%); for Case T1D1, the model underestimated the slip (up to 8%), especially in the later stages. For Case T3D1, the model overestimated the slips (by 34% on average) and advancements (16% on average) in both phases, but estimations on the stride lengths were only slightly overestimated (by 7% on average). These deviations are attributed to the assumptions and simplifications made to derive the model. An important reason may be the fact that the actuator material is not perfectly linearly elastic (Assumption A2). Silicone is in fact a hyper-elastic material in that its modulus decreases with the strain level. For the T3 cases, the modulus used in the model might be lower than that of the material at lower strain levels and, thus, the advancements and slips are overestimated.

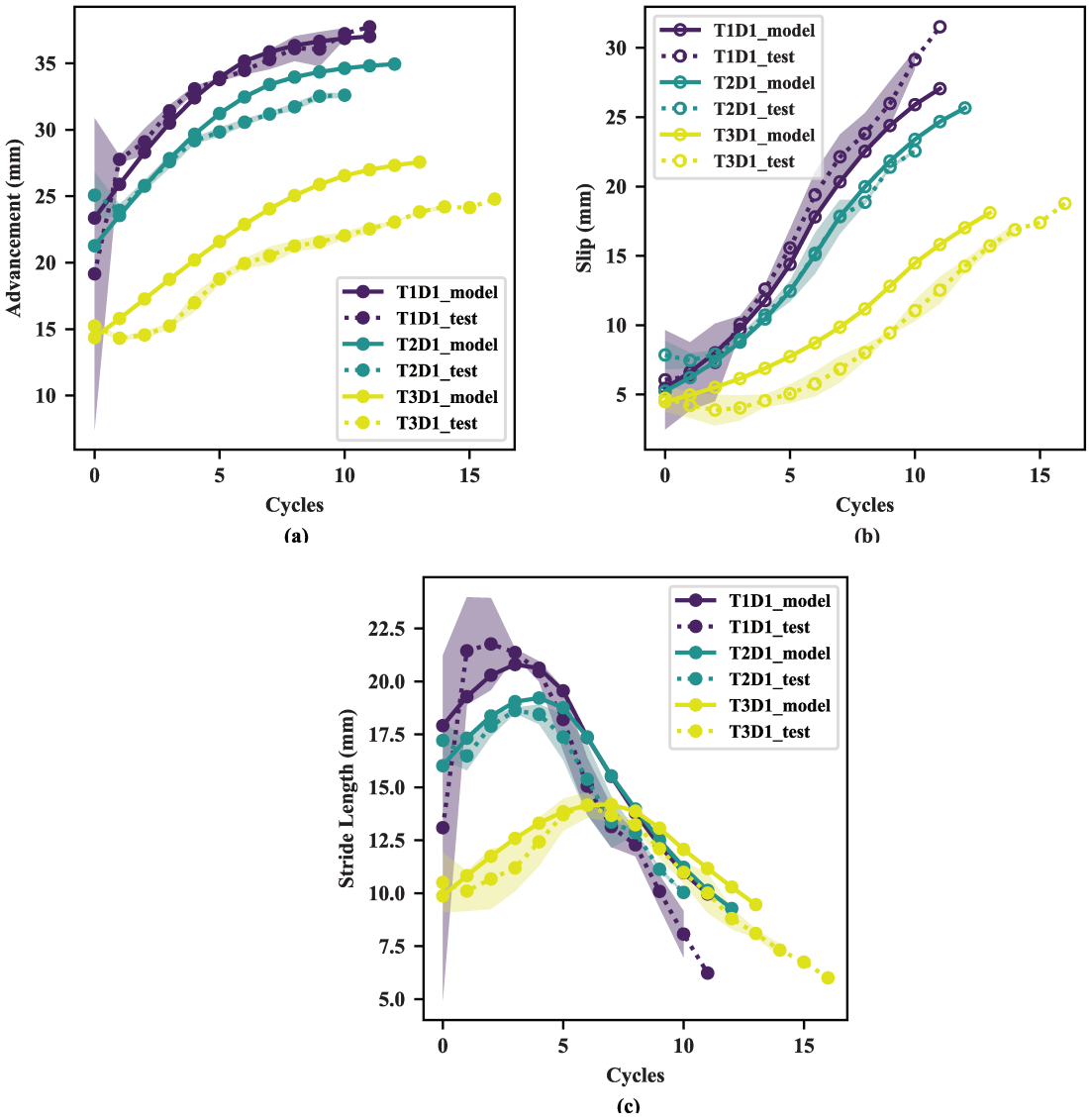

Figure 12. Comparison between the experimental and modeling results for Cases T1D1, T2D1 and T3D1: (a) advancement, (b), slip, and (c) stride length. The curves shown in different colors highlight the effect of actuation period *T*, with T1 = 3.6 s (purple); T2 = 3.0 s (green) and T3 = 1.8 s (yellow). The experimental results are presented using dotted lines (mean values) and shaded bands (standard derivations); the modeling results are presented using solid lines.

4.3 Implications

With this simplified model, we can conduct parametric studies on the effect of each parameter on the burrowing behavior. For example, Figure 13 shows the effects of friction coefficients at the soil–actuator interface. If the upward and downward friction coefficients are the same, as in the tests conducted here, it can be said that the actuator has isotropic friction in both directions. If different, it can then be said that the actuator presents frictional anisotropy. In general, friction plays less and less of a role as the actuator continues to move out of the sand; this is reasonable, since when the actuator is only partially buried, the segment above the ground freely extends/contracts with no influence from the side friction.

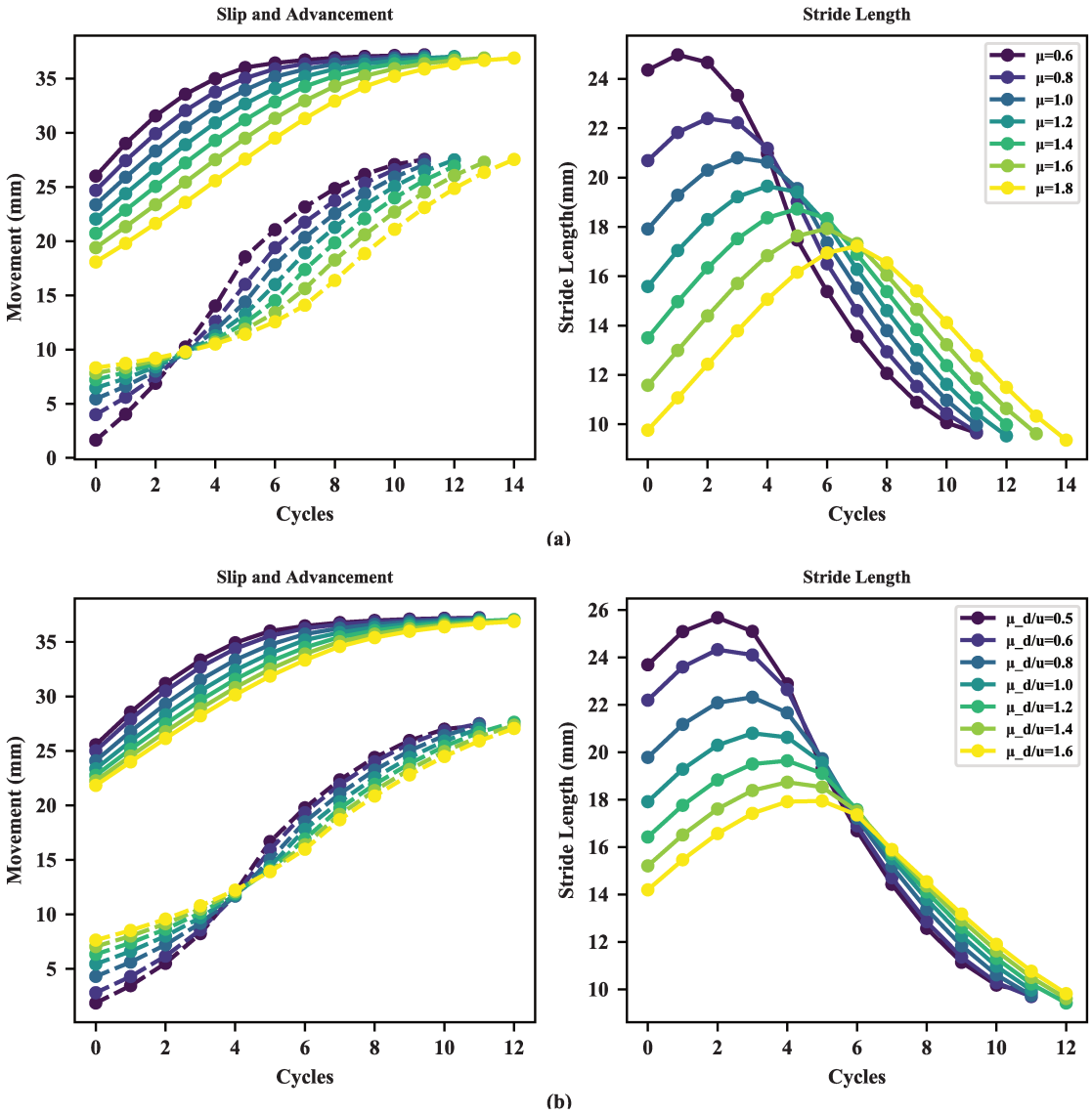

Figure 13. Predicted effects of friction coefficient on burrowing characteristics. (a) Isotropic friction ($\mu_d = \mu_u = \mu$), and (b) anisotropic friction ($\mu_d/\mu_u = \mu$_d/u, $\mu_u = 1$). The curves for advancements and stride lengths are presented using solid lines; the curves for slips are presented using dashed lines.

For cases with isotropic friction (Fig. 13(a)), an increase in the friction coefficient results in shorter advancements in the early cycles; the advancements at the final stage approach to a similar level at the end of the burrowing process, when the majority of the actuator is out of the soil. With a high friction coefficient

(e.g., $\mu = 1.8$), the slip increases slowly in the early stages but more rapidly in the later stages; in contrast, when the friction coefficient is low (e.g., $\mu = 0.6$), the trend is the opposite: the slip begins at a low value and increases rapidly in the early stages, but it slows down at later stages. Overall, lower friction results in greater stride lengths and faster overall burrowing speeds.

Similarly, we can draw conclusions on the effect of frictional anisotropy (Fig. 13(b)). When the downward friction coefficient is greater than the upward friction coefficient (e.g., $\mu_d/\mu_u = 1.6$), the actuator experiences higher resistance during inflation, resulting in smaller advancements; the segment above and below the anchor point also experiences lower and higher resistance during deflation, respectively, resulting in larger slips. The net effect is a significant reduction in stride length in the early stages. On the other hand, if the downward friction coefficient is lower than the upward friction coefficient (e.g., $\mu_d/\mu_u = 0.5$), the anisotropy facilitates the burrowing-out process, leading to greater stride lengths and faster overall burrowing speeds.

Additional parametric studies can be done on the effects of actuator modulus, actuator length, and initial embedment depth (see Supplement S10 for the results). In general, an increase in the actuator modulus reduces the burrowing-out speed (Fig. S4); an increase in the actuator length causes increases in both the advancement and the slip (Fig. S5); and an increase in the embedment depth results in a larger number of cycles required to burrow out of the soil (Fig. S6). In reality, the soil failure modes caused by the uplifting of a circular anchor at a greater depth will be different from those at a shallow depth (see Section 5.2 and Figure 16 for more details). Thus, the uplift capacity factor (N_γ) can no longer be predicted by the value derived for shallow conditions. As such, results from Figure S6 should be interpreted with caution.

5. Discussion

5.1. On the Analytical Model

Many assumptions were made when we developed the analytical model in this study. Some assumptions may become too strong in certain conditions. For example, it was assumed that the anchor point during inflation is at the bottom end of the actuator. However, from the observations made using the 2D chamber and optical flow technique, it was shown that the bottom end of the actuator penetrates downward slightly into the soil at the beginning of the inflation process. The friction coefficient (interface shear strength) between the soil and the actuator was assumed to be constant; it was also assumed that the confining pressure on the actuator equals the at-rest lateral earth pressure. However, it is known in geomechanics and geotechnical engineering that, prior to yielding, the friction coefficient increases; it reaches a peak value if the soil behavior is dilative, and then it remains at a residual level; the confining pressure may also change if the surrounding soil undergoes a change in volume during shearing (dilation or contraction). Further, the soil states were assumed to be unchanged during the burrowing process. In fact, the soil is disturbed considerably during the process, as evidenced by observations of flowing sand around the actuator. Both the lateral confining stress level and the soil state would affect the mobilized friction along the actuator, and the interaction between an actuator and the granular materials would be much more complex, especially with anisotropic frictional features (Huang et al. 2020). Lastly, the elastic behavior of the actuator can be better characterized and described using a nonlinear model (such as a hyperelastic model) to improve the accuracy. Nevertheless, the proposed model predicted the burrowing out behavior well. It is remarkable that the only fitting parameters for the model are for the soil behavior (which is extremely challenging to the model), and all other input parameters were directly measured or readily available. In fact, the fitting parameters were introduced here only to make the model more general; they could have been eliminated from the model if the dilation angles were determined directly.

Unfortunately, the model failed to predict the effects of relative density and saturation. The predicted effect of relative density is shown in Figure 14. Higher relative density only results in slightly lower stride lengths at the early stages. In the experiments with the densest sand (D_r = 69%), however, the actuator first "struggled" to advance significantly for the first 10 cycles (Fig. 10). The exact reason for this phenomenon

is not clear. One hypothesis is that the longer vibrating time required to prepare a sand with a high relative density led to localized soil arching around the actuator, resulting in even denser packing and higher strength and stiffness. The repetitive inflation and deflation of the actuator applied cyclic loading to the surrounding soil. Such cyclic loading probably resulted in a decrease in strength and stiffness of the soil (Martinez et al. 2018) until the actuator "broke through".

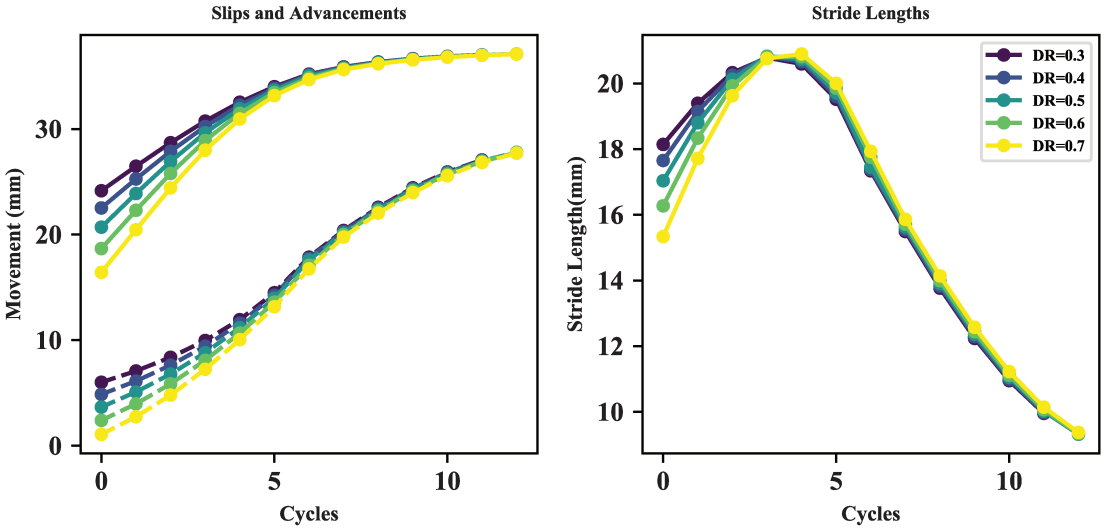

Figure 14. Predicted effects of relative density on burrowing characteristics. The predicted trends were not consistent with the test results shown in Fig. 10.

The predicted effect of soil saturation is shown in Figure 15. In the simulation, the submerged unit weight (γ') was used to calculate the uplift capacity. A reduced interface friction coefficient of 0.8 was used (see Table S3 in the Supplement for test data). With a reduced unit weight of soil, it is expected to that there will be lower friction coefficients, higher stride lengths and faster burrowing speed (Fig. 15). However, the trends in the simulation were the opposite of those observed in the experiments (Fig. 10). This may be attributed to the fact that the downward bearing capacity or penetration resistance of the soil also decreases under a saturated state; in addition, the downward movement (d_{b_in}) of the bottom end of the actuator can be large and non-negligible during the inflation process. It is also possible that an increase in the pore water pressure may have occurred at the two ends of the actuator due to the rapid loading. With increased pore water pressure, the effective stresses decrease, and soil shear strengths would be reduced even further; consequently, the downward displacement may become larger. Another possible explanation is that during the deflation process, a downward suction force may be generated by water underneath the actuator that would lead to less upward movement (d_{b_de}) of the bottom end of the actuator along with greater downward movement (d_{t_de}, slip) of the top end. Changes in d_{b_in} and d_{b_de} would suggest that there are changes in the anchor points; in such a case, Assumption A3 made in the model would no longer be valid, and this would lead to poor predictions for burrowing in saturated sands.

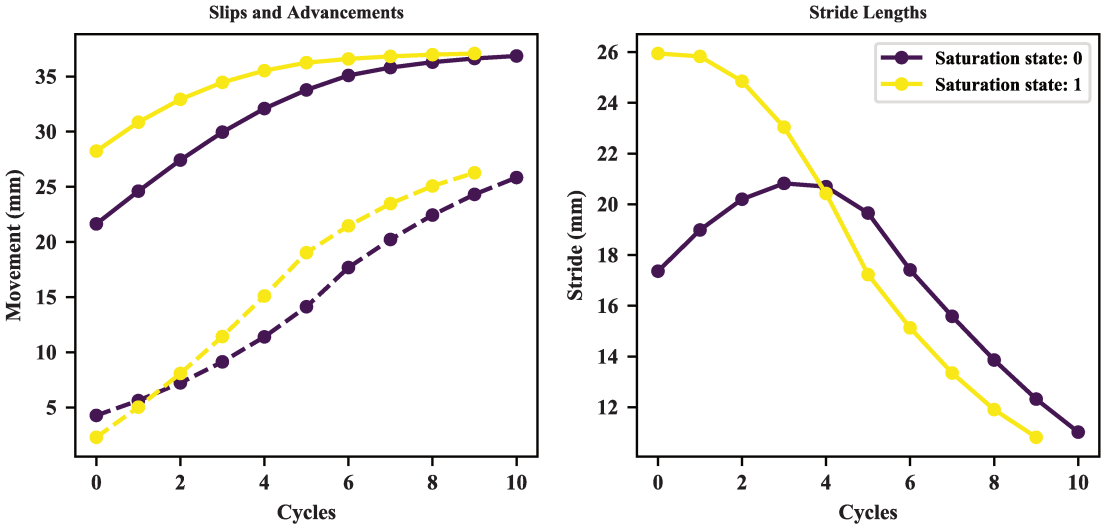

Figure 15. Predicted effects of saturation on burrowing characteristics, where "0" represents the dry state and "1" the saturated state. The predicted trends were not consistent with the test results shown in Fig. 10.

5.2. On Upward Locomotion in Soil

According to Purcell's scallop theorem, for organisms moving in a fluid having a low Reynolds number, if the organism "tries to swim by a reciprocal motion, it can't go anywhere" (Purcell, 1977). In order to obtain net translation, the organism must break the geometric symmetries in the fluid. In addition to geometric symmetries, there are also material asymmetries in certain environments (such as soil). If the material properties are asymmetric, there will be net movement even when the movement itself is reciprocal. It is interesting to compare burrowing in granular materials to swimming in a low-Reynolds-number fluid, since both are largely dominated by drag, and the inertial effect can be disregarded (Hosoi and Goldman 2015). Compared to a low-Reynolds-number fluid environment, the movement in soil can introduce more perturbations to the soil itself and thus change the soil states (stress state or packing). It is noted that there are some common features in natural penetration/burrowing in soil: 1) the organisms periodically change body shapes (e.g., expansion, contraction, extension, undulation) to break the geometric symmetry; 2) the organisms also often modify the soil states around their body (e.g., compaction and fluidization) to break the material/stress symmetry. It is also noted that there are some common features among dual-anchor burrowing, peristaltic burrowing, and root growth/penetration: all three of these mechanisms involve expansion of one part of the body to achieve anchorage and extension (sometimes also contraction) of another part of the body to penetrate the soil. The alternating expansion–extension sequences readily break the geometric symmetry; at the same time, the expansion typically induces compaction of the soil to further increase the anchorage, which breaks the material/stress symmetry.

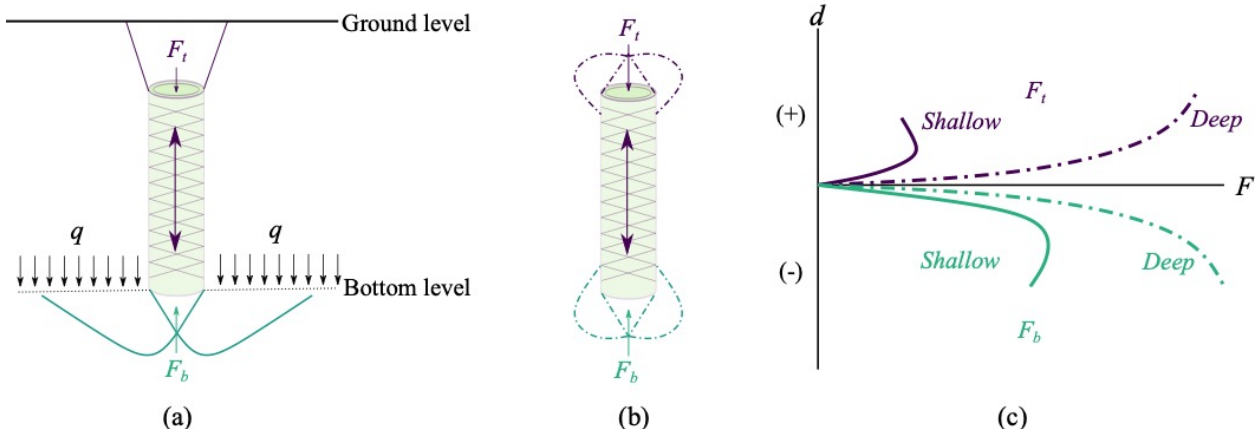

Figure 16. Asymmetric soil failure behaviors: (a) Illustration of soil failure surfaces at both ends of the actuator at shallow embedment depths; q is the equivalent surface loading, which is due to the self-weight of the soil above the bottom level. (b) localized soil failure surfaces at deep embedment depths; and (c) diagram showing the mobilization of the end bearing force F with end displacement d. Positive d indicates upward movement and the corresponding end bearing force is denoted by F_t; negative d indicates downward movement and the corresponding end bearing force is denoted by F_b. In the figures, solid and dashed lines are consistently used for shallow conditions and deep conditions, respectively.

Unlike the downward burrowing process that mainly relies on the dual-anchor burrowing mechanism, the upward burrowing process of razor clams only involves largely symmetric and reciprocating extension and contraction of the foot. This reciprocal motion indeed results in net movement—not because of the asymmetric geometry but due to the inherent asymmetric behavior of the soil (Figure 16). Due to the gravitational effect, soil deposit vertically and the stress level increases with depth. This inherent soil anisotropy is also believed to be the cause for the drag induced lift in granular materials (Ding et al. 2011). In contrast to a fluid, which cannot sustain any shear stress, soils rely mainly on shearing resistance to prevent failure. The shear strength comes from interparticle cohesion and friction. The frictional forces are stress-dependent: the higher the confining stress, the higher the frictional strength. When an object moves in soil, the resistance comes from the shear strength of the soil on the failure surface as well as any contribution from the weight of soil. A critical depth exists, which leads to the categorization of different failure mechanisms into shallow (Fig. 16a) and deep (Fig. 16b) conditions. This critical depth depends on the direction of movement (upward/downward), the soil properties, and the geometry of the moving object. At shallow depths (Fig. 16a), the failure surfaces for upward movement extend to the ground level; the total upward resistance is always smaller than the total downward resistance, due to both a higher stress level and a larger failure surface area for downward failure. In other words, it is easier to move upward than downward at a shallow depth. At greater depths (Fig. 16b), the failure surfaces for upward and downward movements are both localized; although the difference in the stress level may be the same as at a shallow depth, the difference in the failure surface area decreases. As a result, the upward resistance and downward resistance approach a similar level at the critical depth (Fig. 16c); the difference between these two becomes small comparing to the resistances themselves. Therefore, it would be challenging for an object to move upward effectively if it only relies on reciprocal motion at deep depths.

The rapid upward burrowing process observed in the tests is also attributed to the backfilling phenomena that occurs during the deflation process due to flowing nature of the dry sand upon yielding (Section 3.4.2). The void beneath of the bottom end of the actuator that results from deflation is filled with sand, which provides a new baseline for the subsequent actuation cycle. For highly cohesive soils where the wall of the void may become stable due to cohesion, the upward burrowing process maybe inhibited, since a newly elevated base would not be able to form during the deflation process.

5.3. On Bio-inspired Self-burrowing Robots

In order for an organism to burrow downward, the anchorage should be higher than the penetration resistance. This can be achieved by increasing the anchorage or by decreasing the penetration resistance—or, ideally, by both. The dual-anchor mechanism increases anchorage through the expansion of the body, which increases both the contact surface area and the confining pressure; part of the anchorage resistance also comes from the end bearing from the top end. On the other hand, the penetration resistance is decreased by shrinking the body, which not only decreases the contact surface area but may also fluidize the surrounding soil (Winter et al. 2012); the organisms may also have evolved with streamlining features (such as a curved body or a structure having a pointy tip), which can possibly be leveraged to reduce penetration resistance. In nature, other mechanisms exist to increase anchorage, for example, by roughening the body surfaces with setae, scales, or root hairs. Other fluidization methods can also be found: for example, water jetting, vibration or rotation. All of these natural burrowing mechanisms can inspire designs for future self-burrowing robots.

6. Conclusions

We observed that the Atlantic razor clam (*Ensis directus*) adopts a different strategy for upward burrowing from the one it uses for downward burrowing. The upward burrowing process mainly consists of periodic extension and retraction of the foot. This locomotion gait is considered to be different from—and simpler than—the downward burrowing gait, which includes shell expansion, foot extension, shell contraction, foot dilation, and shell retraction. Inspired by the upward burrowing mechanism of razor clams, we designed a minimalistic self-burrowing robot that burrows out of sand naturally when it extends and contracts under pneumatic inflation/deflation. During the upward burrowing process, the stride length first increases due to a drop in the overburden pressure, the end pull-out resistance, and the side frictional resistance from the soil; the stride length then decreases once the top of the actuator is above the soil surface, due to a reduction in the effective length of the actuator.

We show that effective upward burrowing with a vertical reciprocating motion in sand is due to two major reasons: 1) the intrinsically asymmetric material properties and stress states in a sand deposit readily break down the symmetry, as required for locomotion; and 2) the flowing nature of sand upon yielding allows a new elevated baseline to form after each cycle. We proposed a simplified analytical model based on soil mechanics to explain the observed burrowing behaviors of the robot. The model featured the soil- and depth-dependent uplift capacity of a circular plate, the soil- and actuator material–dependent interface friction, as well as the elasticity of the actuator itself. The model predicted the effects of inflation/deflation pressure remarkably well. Improvements are needed to better predict the effects of relative density (especially for the dense cases), saturation, and embedment depth. The effects of interface friction (especially interface anisotropy), modulus and length that are predicted by the model can shed light on the design of future burrowing robots. While upward burrowing is natural due to the intrinsic asymmetry of material properties of soil, downward burrowing is more challenging and may require the robot to break symmetries in geometry, material properties and stress states, as is the case for many natural burrowing processes.

Acknowledgements

This material is based upon work primarily supported by the National Science Foundation (NSF) under NSF Award Nos. CMMI-1841574, CMMI-1849674 and EEC-1449501. Any opinions, findings and conclusions, or recommendations expressed in this paper are those of the author(s) and do not necessarily reflect those of NSF. The authors also wish to thank Professor Dale Levitt at Roger Williams University for his help in harvesting the razor clams and his advice on maintaining the aquarium at ASU. We also thank ASU undergraduate research assistant Alexandra Ardente for helping in the fabrication of the actuator.

References

Abdalla A., Hettiaratchi D., and Reecea A. 1969. The mechanics of root growth in granular media. *Journal of Agricultural Engineering Research,* 14**,** 236–248.

Abraham Y. and Elbaum R. 2013. Hygroscopic movements in Geraniaceae: the structural variations that are responsible for coiling or bending. *New Phytologist,* 199**,** 584–594.

Ansell A. D. 1967. Leaping and other movements in some cardiid bivalves. *Animal Behaviour,* 15**,** 421–426.

Ansell A. D. and Trevallion A. 1969. Behavioural adaptations of intertidal molluscs from a tropical sandy beach. *Journal of Experimental Marine Biology and Ecology,* 4**,** 9–35.

Bengough A.G., Mullins C.E. and Wilson G. 1997. Estimating soil frictional resistance to metal probes and its relevance to the penetration of soil by roots. *European Journal of Soil Science*, 48, 603-612

Bolton M. 1986. Strength and dilatancy of sands. *Geotechnique,* 36**,** 65–78.

Bradski G. and Kaehler A. 2000. The OpenCV Library. *Dr. Dobb's Journal of Software Tools,* 3.

Chakraborty T. and Salgado R. 2010. Dilatancy and shear strength of sand at low confining pressures. *Journal of Geotechnical and Geoenvironmental Engineering,* 136**,** 527–532.

Che J. and Dorgan K. M. 2010. Mechanics and kinematics of backward burrowing by the polychaete Cirriformia moorei. *Journal of Experimental Biology,* 213**,** 4272–4277.

Connolly F., Polygerinos P., Walsh C. J. and Bertoldi K. 2015. Mechanical programming of soft actuators by varying fiber angle. *Soft Robotics,* 2**,** 26–32.

D'Aoüt K. And Aerts P. 1999. A kinematic comparison of forward and backward swimming in the eel Anguilla anguilla. *Journal of Experimental Biology,* 202**,** 1511–1521.

Del Dottore E., Mondini A., Sadeghi A. and Mazzolai B. 2018. Swarming Behavior Emerging from the Uptake–Kinetics Feedback Control in a Plant-Root-Inspired Robot. *Applied Sciences,* 8**,** 47.

Ding Y., Gravish N. and Goldman D. 2011 Drag Induced Lift in Granular Media. *Physical Review Letters*, 106, 028001.

Dorgan K. M. 2015. The biomechanics of burrowing and boring. *Journal of Experimental Biology,* 218**,** 176–183.

Drew G. A. 1907. The Habits and Movements of the Razorshell Clam, Ensis Directus, Con. *The Biological Bulletin,* 12**,** 127–140.

Eilam D. Adijes M. and Vilensky J. 1995. Uphill locomotion in mole rats: a possible advantage of backward locomotion. *Physiology & Behavior,* 58**,** 483–489.

Eilam D. And Shefer G. 1992. Reversal of interleg coupling in backward locomotion implies a prime role of the direction of locomotion. *Journal of Experimental Biology,* 173**,** 155–163.

Evangelista D., Hotton S. And Dumais J. 2011. The mechanics of explosive dispersal and self-burial in the seeds of the filaree, Erodium cicutarium (Geraniaceae). *Journal of Experimental Biology,* 214**,** 521–529.

Farnebäck G. 2003. Two-frame motion estimation based on polynomial expansion. Scandinavian Conference on Image Analysis. Springer, Berlin, Heidelberg, 363–370.

Fraenkel, G. S. 1927. Die Grabbewegung der Soleniden. *Fisheries Research Board of Canada,* 6**,** pp.168–220.

Gao Y. Ellery A., Jaddou M., Vincent J. and Eckersley S. 2007. Planetary micro-penetrator concept study with biomimetric drill and sampler design. *IEEE Transactions on Aerospace and Electronic Systems,* 43**,** 875–885.

Giampa J. R. and Bradshaw A. S. 2018. A simple method for assessing the peak friction angle of sand at very low confining pressures. *Geotechnical Testing Journal,* 41**,** 639–647.

Giampa J. R., Bradshaw A. S. and Schneider J. A. 2016. Influence of dilation angle on drained shallow circular anchor uplift capacity. *International Journal of Geomechanics,* 17**,** 04016056.

Herrel A., Choi H. F., Dumont E., De Schepper N., Vanhooydonck B., Aerts P. and Adriaens D. 2011. Burrowing and subsurface locomotion in anguilliform fish: behavioral specializations and mechanical constraints. *Journal of Experimental Biology,* 214**,** 1379–1385.

Hettiaratchi D. and Ferguson C. 1973. Stress-deformation behaviour of soil in root growth mechanics. *Journal of Agricultural Engineering Research* 18, 309–320.

Holland D. P., Park E. J., Polygerinos P., Bennett G. J. and Walsh C. J. 2014. The soft robotics toolkit: Shared resources for research and design. *Soft Robotics,* 1**,** 224–230.

Hosoi A. and GoldmAN D. I. 2015. Beneath our feet: strategies for locomotion in granular media. *Annual Review of Fluid Mechanics,* 47**,** 431-453.

Huang S., Mahabadi A.M., and Tao J. 2020 Impact of shell-opening of a model razor clam on the evolution of force chains in granular media, *Geo-Congress 2020* DOI: 10.1061/9780784482834.030

Huang S., Tang Y., Bagheri H., Li D., Ardente A., Aukes D., Marvi H., and Tao J. 2020. Effects of Friction Anisotropy on Upward Burrowing Behavior of Soft Robots in Granular Materials. *Advanced Intelligent Systems.* doi: 10.1002/aisy.201900183

Huang S. and Tao J. 2018 The interplay between shell opening and foot penetration of a model razor clam: Insights from DEM simulation, *B2G Atlanta 2018: Bio-mediated and Bio-inspired Geotechnics*

Huang S. and Tao J. 2020 Modeling Bio-inspired Burrowing in Dry Sand using Cavity Expansion Theory and DEM, *Acta Geotechnica* DOI:10.1007/s11440-020-00918-8

Isaka K., Tsumura K., Watanabe T., Toyama W., Sugesawa M., Yamada Y., Yoshida, H. and Nakamura, T. 2019. Development of Underwater Drilling Robot Based on Earthworm Locomotion. *IEEE Access,* 7**,** 103127–103141.

Jones C. G., Lawton J. H. and Shachak M. 1997. Positive and negative effects of organisms as physical ecosystem engineers. *Ecology,* 78**,** 1946–1957.

Jung S. 2010. Caenorhabditis elegans swimming in a saturated particulate system. *Physics of Fluids,* 22**,** 031903.

Jung W., Choi S. M. Kim W. and Kim, H.-Y. 2017. Reduction of granular drag inspired by self-burrowing rotary seeds. *Physics of Fluids,* 29**,** 041702.

Liu B., Ozkan-Aydin Y., Goldman D. I. and Hammond F. L. 2019. Kirigami Skin Improves Soft Earthworm Robot Anchoring and Locomotion Under Cohesive Soil. 2019 2nd IEEE International Conference on Soft Robotics (RoboSoft), Seoul, Korea, 828–833.

Lucas B. D. and Kanade T. 1981. An iterative image registration technique with an application to stereo vision; Proceedings of the 7th International Joint Conference on Artificial Intelligence, Vancouver, B.C., Canada. Pages 674–679.

Maladen R. D., Ding Y., Li C. and Goldman D. I. 2009. Undulatory swimming in sand: subsurface locomotion of the sandfish lizard. *Science,* 325**,** 314–318.

Martinez A., O'Hara K.B., Sinha S.K., Wilson D., and Ziotopoulou K. 2018. Monotonic and Cyclic Centrifuge Testing of Snake Skin-Inspired Piles. *Proceedings of Biomediated and Bioinspired Geotechnics (B2G) Conference*, Atlanta, USA.

Mazzolai B., Mondini A., Corradi P., Laschi C., Mattoli V., Sinibaldi E. and Dario P. 2010. A miniaturized mechatronic system inspired by plant roots for soil exploration. *IEEE/ASME Transactions on Mechatronics,* 16**,** 201–212.

Naclerio N. D., Hubicki C. M., Aydin Y. O., Goldman D. I. and Hawkes E. W. 2018. Soft robotic burrowing device with tip-extension and granular fluidization. 2018 IEEE/RSJ International Conference on Intelligent Robots and Systems (IROS), Madrid, Spain, 5918–5923.

Nash R., Chapman C., Atkinson R. and Morgan P. 1984. Observations on the burrows and burrowing behaviour of *Calocaris macandreae* (Crustacea: Decapoda: Thalassinoidea). *Journal of Zoology,* 202**,** 425–439.

Ortiz D., Gravish N. and Tolley M. T. 2019. Soft Robot Actuation Strategies for Locomotion in Granular Substrates. *IEEE Robotics and Automation Letters,* 4**,** 2630–2636.

Ozkan-Aydin Y., Murray-Cooper M., Aydin E., Mccaskey E. N., Naclerio N., Hawkes E. W. and Goldman, D. I. 2019. Nutation Aids Heterogeneous Substrate Exploration in a Robophysical Root. 2nd IEEE International Conference on Soft Robotics (RoboSoft), Soeul, Korea, 172–177.

Pitcher C. and Gao Y. 2015. Analysis of drill head designs for dual-reciprocating drilling technique in planetary regoliths. *Advances in Space Research,* 56**,** 1765–1776.

Polygerinos P., Correll N., Morin S. A., Mosadegh B., Onal C. D., Petersen K., Cianchetti M., Tolley M. T. and Shepherd R. F. 2017. Soft robotics: Review of fluid-driven intrinsically soft devices; manufacturing, sensing, control, and applications in human-robot interaction. *Advanced Engineering Materials,* 19**,** 1700016.

Purcell E. M. 1977. Life at low Reynolds number. *American Journal of Physics,* 45**,** 3–11.

Quillin K. 2000. Ontogenetic scaling of burrowing forces in the earthworm Lumbricus terrestris. *Journal of Experimental Biology,* 203**,** 2757–2770.

Quillin K. J. 1999. Kinematic scaling of locomotion by hydrostatic animals: ontogeny of peristaltic crawling by the earthworm Lumbricus terrestris. *Journal of Experimental Biology,* 202**,** 661–674.

Rafeek S., Gorevan S., Bartlett P. and Kong, K. 2001. The inchworm deep drilling system for kilometer scale subsurface exploration of Europa (IDDS). Forum on Innovative Approaches to Outer Planetary Exploration 2001–2020, Houston, Texas. 68.

Sadeghi A., Tonazzini A., Popova L. and Mazzolai B. 2014. A novel growing device inspired by plant root soil penetration behaviors. *PloS One,* 9**,** e90139.

Sapir N. and Dudley R. 2012. Backward flight in hummingbirds employs unique kinematic adjustments and entails low metabolic cost. *Journal of Experimental Biology,* 215**,** 3603–3611.

Tang Y., Huang S. and Tao J. 2020 Effect of rotation on seed's self-burial process: insights from DEM simulations, *Geo-Congress 2020* DOI: 10.1061/9780784482834.032

Tao J., Huang S. and Tang Y. 2019. Bioinspired Self-Burrowing-Out Robot in Dry Sand. *Journal of Geotechnical and Geoenvironmental Engineering*, 145 (12), 02819002

Tatom‐Naecker T. A. M. and Westneat M. W. 2018. Burrowing fishes: Kinematics, morphology and phylogeny of sand-diving wrasses (Labridae). *Journal of Fish Biology,* 93**,** 860–873.

Trueman E. 1967. The dynamics of burrowing in Ensis (Bivalvia). *Proceedings of the Royal Society of London. Series B. Biological Sciences,* 166**,** 459–476.

Trueman E. 1971. The control of burrowing and the migratory behaviour of Donax denticulatus (Bivalvia: Tellinacea). *Journal of Zoology,* 165**,** 453–469.

Trueman E. 1983. Locomotion in molluscs. In *The Mollusca, Vol. 4.* Saleuddin A.S.M. and Wilbur K.M., eds. Academic Press (Elsevier), Cambridge, Mass. USA. pp. 155–198

Trueman E., Brand, A. and Davis, P. 1966. The dynamics of burrowing of some common littoral bivalves. *Journal of Experimental Biology,* 44**,** 469–492.

Winter A., Deits R., Dorsch D., Slocum A. and Hosoi A. 2014. Razor clam to RoboClam: burrowing drag reduction mechanisms and their robotic adaptation. *Bioinspiration and Biomimetics,* 9**,** 036009.

Winter A. G., Deits R. L. and Hosoi A. E. 2012. Localized fluidization burrowing mechanics of Ensis directus. *Journal of Experimental Biology,* 215**,** 2072–2080.